

Etching of diamond in hydrogen

James King

Supervisor:
Professor P.W. May

Second Assessor:
Dr N.A. Fox

April 2013



Submitted in partial fulfilment of the
requirements for the Honours degree
of MSci in Chemistry

Abstract

The etching of diamond by atomic hydrogen is a crucial process that occurs during diamond growth by chemical vapour deposition (CVD). The purpose of this thesis was to investigate the etching of the (100) diamond surface, looking at the relative etch rates of diamond and graphite, comparing the etch rates parallel and perpendicular to the diamond surface, and looking into the mechanism by which atomic hydrogen removes carbon from the surface.

All etching was undertaken using a microwave CVD reactor. The graphite-diamond etch rate comparison used polycrystalline diamond samples and graphite disks. The etch rates were calculated using the mass loss over the etching period, taking the surface area of the sample into account, varying the reactor pressure. Preliminary results showed that graphite etches 200 times faster than diamond at 100 Torr, but problems with the setup prevented further investigation.

The lateral-vertical etch rate investigation was carried out using single crystal diamond samples and the effect of changing the pressure was investigated. Atomic force microscopy was used to analyse square etch pits formed on the surface, the geometries of which were used to calculate the relative etch rates. A lateral to vertical etch rate ratio of 7:1 was found at 100 Torr, and the ratio was found to decrease as pressure increased. It was also shown that the diamond surface goes through a cycle of phases, involving the formation of etch pits followed by the rapid lateral etching of entire layers to produce a smooth surface, on which fresh etch pits form. These observations agree with many previous theories on the anisotropic etching of the (100) diamond surface, with lateral etching being facile once a defect is formed within a diamond layer.

Finally a combination of semi-empirical PM3 calculations and density functional theory calculations were used to successfully model a mechanism by which carbon is removed from a reconstructed dimer on the (100) diamond surface, in the form of methyl radical, via a series of atomic hydrogen additions, abstractions and structural rearrangements. The energy minima and transition states were successfully calculated, and the magnitude of the individual steps were in line with a process that is possible under CVD conditions, but at the slow rate expected of diamond etching. The energetic of this mechanism, when applied to various surface features, can potentially help explain many of the experimentally observed phenomenon and relative etch rates of the individual features.

Table of Contents

Abstract	2
List of Figures	5
List of Tables	7
CHAPTER 1 – INTRODUCTION	8
1.1 Physical Properties of Diamond	8
1.2 Diamond Growth by Chemical Vapour Deposition	10
1.3 Etching of Diamond by Atomic Hydrogen	11
1.3.1 Preferential Etching of Under-Coordinated Carbon	13
1.3.2 Anisotropic Etching	15
1.4 Aim of the Study	17
1.5 References	18
CHAPTER 2 – EXPERIMENTAL	20
2.1 The Microwave Reactor	20
2.2 Atomic Force Microscopy	22
2.3 Diamond and Graphite Etch Rate Comparison	23
2.4 Lateral and Vertical Etch Rate Comparison	23
2.5 Computational Studies into the Mechanism of Etching	24
2.6 References	25
CHAPTER 3 – RESULTS AND DISCUSSION	26
3.1 Diamond and Graphite Etch Rate Comparison	26
3.2 Lateral and Vertical Etch Rate Comparison	27
3.3 Computational Studies into the Mechanism of Etching	34
3.3.1 Semi-Empirical (PM3) Calculations	35
3.3.2 Density Functional Theory (DFT) Calculations	37
3.4 References	40
CHAPTER 4 – AFTERWORD	41

4.1.	Conclusion.....	41
4.2.	Future Work.....	41
4.3.	Acknowledgements.....	42
4.4.	References	43
	APPENDICES.....	44

List of Figures

- Figure 1.1 *The structure of the diamond unit cell^[3].*
- Figure 1.2 *The (100), (111) and (110) diamond surfaces^[10]*
- Figure 1.3 *The general mechanism for CVD in a hot filament reactor. Gases are activated by the hot filament (or electron bombardment in the plasma for microwave reactors) before diffusing to the substrate surface, forming a diamond film under the correct conditions^[12].*
- Figure 1.4 *(a) STM image of etch pits on a (100) diamond film after exposure to atomic hydrogen for 12 min at 500°C^[35]. (b) STM image of a non-hydrogen terminated diamond (100) surface after atomic hydrogen exposure for 5 min at 1000°C. S_A , S_B and D_A steps, along with some dimer rows, are clearly visible and examples are labelled^[33].*
- Figure 1.5 *SEM images showing square (100) facets and triangular (111) facets on two samples of CVD diamond^[10]*
- Figure 1.6 *The mechanism for the adsorption and incorporation of a methyl radical on a 2 x 1(100) diamond surface, leading to growth^[27].*
- Figure 1.7 *The mechanism for the etching of a methyl radical from a diamond 2 x 1 (100) surface by atomic hydrogen^[27].*
- Figure 1.8 *A schematic diagram of the top-down view of a 2 x 1 (100) diamond surface. The large, middle and small sized circles represent carbon atoms in the top, second and third layers respectively. Shaded circles represent carbon atoms which are hydrogen terminated. S_A steps run parallel to dimer rows, whilst S_B steps run perpendicular to them^[33].*
- Figure 1.9 *The Infrared spectra of C-H stretches as a function of hydrogen etching time of 3,4,5 and 8h (a-d) for the (100) surface and 3,7,8 and 9h (e-h) for the (110) surface. C-H stretches in the 2920 cm⁻¹ range can be assigned to (100) facets, the singlet peak at 2830 cm⁻¹ assigned to (111) facets, and the signal at 2850-2870 cm⁻¹ assigned to (110) facets^[41].*
- Figure 2.1 *The MWCVD apparatus used for diamond etching^[1]. Labelled parts: (a) MW magnetron, (b) MW waveguide, (c) optical pyrometer, (d) reactor chamber, (e) water cooling circulation pipes, (f) process gas inlet, (g) viewing window, (h) gas exhaust, (i) air cooling pipe, (j) solenoid valve, (k) pressure regulating butterfly valve.*
- Figure 2.2 *The AFM apparatus used for surface characterisation. Labelled parts: (a) Light source, (b) Control box, (c) Microscope, (d) Laser source, (e) Cantilever head, (f) Cantilever, (g) Sample stage.*
- Figure 2.3 *A ball and stick representation of the $C_{17}H_{22}$ cluster used to model the H-terminated, 2x1 (100) reconstructed diamond surface.*
- Figure 2.4 *A ball and stick representation of the $C_{97}H_{74}$ cluster used to model the H-terminated, 2x1 (100) reconstructed diamond surface. The two images are at 90° to each other, clearly showing the lone carbon dimer on the top, and the dimer rows of the layer below.*
- Figure 3.1 *Plot of diamond etch rate per unit area as a function of reactor pressure (p).*

- Figure 3.2 *A pre-etch AFM image of a polished SCD sample. The average surface roughness is 1.3442 nm. Mechanical polishing scratch lines can be seen across the surface, along with the some small surface defect.*
- Figure 3.3 *A 5 x 5 μm AFM picture of sample 1 post-etch, in 2D and 3D. The picture shows many square etch pits of roughly the same size.*
- Figure 3.4 *A 5 x 5 μm AFM picture of sample 2 post-etch, in 2D and 3D. Large steps can be seen, being etched away to leave a smoother surface. The straight sides to the steps are D_A steps, whilst the rougher sides are a series of S_B edges.*
- Figure 3.5 *A 5 x 5 μm AFM picture of sample 3 post-etch, in 2D and 3D. Samples of the small etch pits are highlighted with arrows.*
- Figure 3.6 *A 5 x 5 μm AFM picture of sample 4 post-etch, in 2D and 3D. Only a small amount of etching has occurred around the surface defects.*
- Figure 3.7 *Two 5 x 5 μm images of sample 5. All images showed the diamond surface to be covered in a range of unknown features. It is possible to see some square etch pit like shapes on both of these images.*
- Figure 3.8 *A 5 x 5 μm AFM picture of sample 6 post-etch, in 2D and 3D. The picture shows several large etch pits, some of which overlap. In the top right it is possible to see that two etch pits have collided, and the upper layers surrounding the point of collision have begun to etch away rapidly across the surface.*
- Figure 3.9 *Plot of the lateral : vertical etch rate ratio as a function of pressure (p).*
- Figure 3.10 *The proposed etching mechanism.*
- Figure 3.11 *The potential energy surface (PES) illustrating the rearrangement of a reconstructed dimer on a diamond (100) surface (**a**) to a dangling carbon double bond (**h**), prior to removal of a methyl radical, modelled using PM3 level calculations and the smaller cluster (figure 2.3). The energies are in kJ mol^{-1} relative to **a** (137 kJ mol^{-1}). Optimised structure energies are in blue and transition states are in orange.*
- Figure 3.12 *The potential energy surface (PES) illustrating the rearrangement of a reconstructed dimer on a diamond (100) surface (**a**) to a dangling carbon double bond (**h**), prior to removal of a methyl radical, modelled using PM3 level calculations and the bigger cluster (figure 2.4). The energies are in kJ mol^{-1} relative to **a** (1450 kJ mol^{-1}). Optimised structure energies are in blue and transition states are in orange.*
- Figure 3.13 *The potential energy surface (PES) illustrating the rearrangement of a reconstructed dimer on a diamond (100) surface (**a**) to a dangling carbon double bond (**h**), followed by the removal of a methyl radical (**k**), modelled using DFT. The energies are in kJ mol^{-1} relative to **a**. Optimised structure energies are in blue and transition states are in orange. Starting energy of **a** = $-1.74 \times 10^6 \text{ kJ mol}^{-1}$*
- Figure 3.14 *An example of a diamond QM/MM model, showing the large MM region (diamond lattice) and the small central QM region (ball and stick C_9H_{14} cluster) used to model a lone dimer on the diamond (100) surface.*

List of Tables

- Table 2.1 *Etch conditions P , F , p , t , T , and the sample surface area A for PCD samples A and B, and Graphite sample A.*
- Table 2.2 *Etch conditions P , F , p , t , T , and the sample dimensions d for samples A-G.*
- Table 3.1 *The rate of mass loss per unit area for the three successful runs, along with the pressures they were run at. Other run conditions can be seen in Table 2.1.*
- Table 3.2 *The etch pit density, dimensions and the etch rate ratios for Samples **1**, **3** and **6**.*

Chapter 1 – Introduction

1.1 Physical Properties of Diamond

Diamond is an allotrope of carbon, composed of sp^3 -hybridized carbon atoms covalently bonded to four neighbouring carbon atoms in a tetrahedral lattice (*figure. 1.1*). Diamond has many unique properties, both mechanical and chemical, that make it a very interesting material on top of its natural beauty. Due to the strong covalent bonding and its three-dimensional lattice, diamond possesses an extremely stable structure, high fracture toughness^[1], low friction coefficient and is the hardest natural material according to the Mohs scale of mineral hardness (it has a bulk modulus of $4.4 \times 10^{11} \text{ N/m}^2$, more than four times that of silicon). These mechanical properties make diamond ideal for use as a wear resistant coating for cutting and machine tools, and as an abrasive. Diamond also has a high thermal conductivity of $15 \times 10^3 \text{ W/m}^2\text{K}^{-1}$, a high optical dispersion^[2] and is optically transparent to radiation from the ultraviolet to the far infrared, making diamond a useful material for heat sinks, lenses and laser windows. Its stability gives diamond extreme chemical inertness making it highly resistant to degradation and, consisting of just carbon, it is biocompatible creating potential applications within the human body^[3]. These properties apply to single crystal diamond (SCD), but within research and industry it is often more simple and cheaper to grow polycrystalline diamond (PCD) films. PCD primarily consists of many small diamond crystals that grow together into a film. They often have high concentrations of defects and increasing quantities of non-diamond carbon phases, such as graphite, as the average crystal size decreases. These polycrystalline films are generally slightly weaker than single crystal films and natural diamond^[4] but still retain many of the properties associated with single crystal diamond.

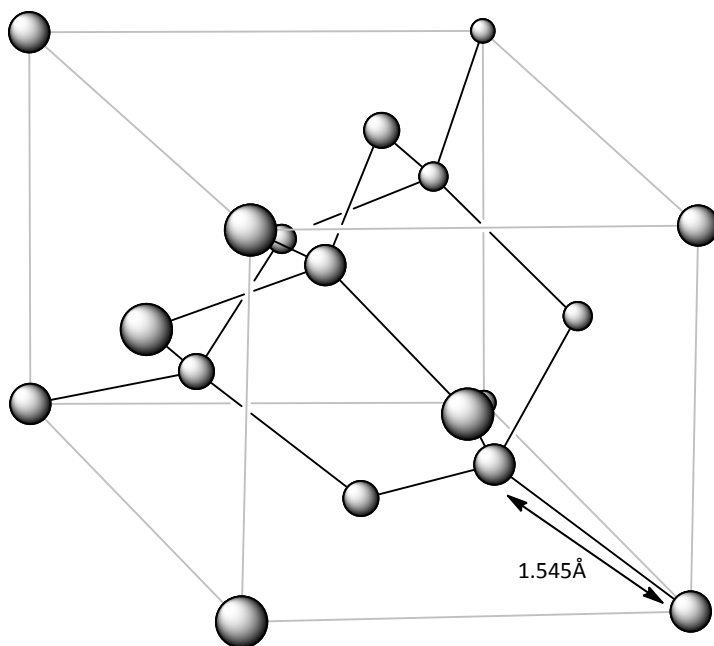


Figure 1.1: The structure of the diamond unit cell^[3].

The morphology of the diamond surface varies depending on the way the cubic diamond unit cell is cut. The most common stable diamond crystal faces can be described as the (100), (110) and (111) surfaces (*figure 1.2*) determined by how they intercept the perpendicular axes (x, y, z) and assigned a Miller index. Many of the surface properties of diamond are anisotropic^[4], differing for each diamond surface orientation. The rate of oxidation of the (111) surface is approximately 10 times that of the (100) surface^[5], and theoretical energy required to cleave diamond on the (111) surface is almost half that required for the (100) surface^[6]. The (111) plane is the most common facet in both synthetic and natural diamond, followed by (100) and finally (110). The (100) surface usually forms a 2×1 reconstructed form, in which two carbon atoms at the surface relax from the bulk positions, moving together to form a C-C bond in the plane of the surface to saturate the dangling bonds at the surface. These dimers form long rows along the surface^[7-9]. The remaining dangling bond is usually terminated by hydrogen, maintaining the tetrahedral structure.

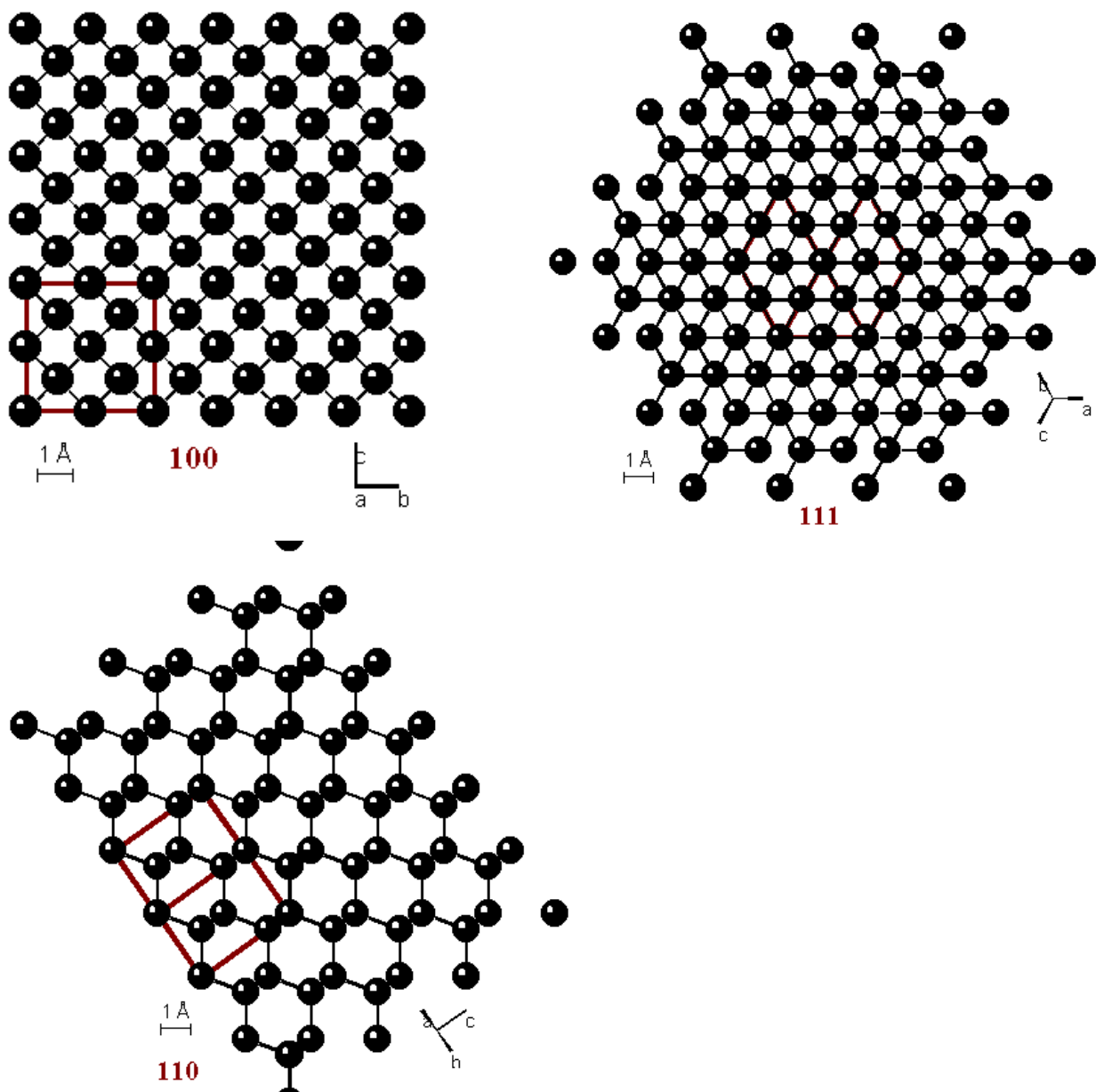


Figure 1.2: The (100), (111) and (110) diamond surfaces^[10]

1.2 Diamond Growth by Chemical Vapour Deposition

The most common method used in industry to create synthetic diamond uses high pressures and temperatures, mimicking the conditions natural diamond forms under. These high-pressure, high-temperature (HPHT) methods use pressures of around 100,000 atm, temperatures around 2500K and a molten metal catalyst to create diamond^[11]. Since it is the denser allotrope of carbon, diamond is more stable under these extreme conditions, rather than the more common allotrope, graphite. These methods tend to form a powder of single crystal diamonds with sizes ranging from micrometers (μm) to millimetre (mm).

Chemical vapour deposition (CVD) is a newer method for diamond growth. CVD gets rid of the extreme conditions required for HPHT, lowering costs, and allows smooth diamond films to be formed. This method involves a gas phase reaction, typically a mixture of hydrogen and a carbon containing precursor molecule (usually methane), above a substrate causing deposition onto the substrate surface. To initiate growth the feed gases must be activated. This is often done using thermal energy (within a hot filament reactor) or via plasma activation (within a microwave reactor), forming the reactive species required for growth, methyl radicals and atomic hydrogen. Whilst the method of activation differs for each approach, other features are all common. For diamond growth gas pressures are very low and a wide range of temperatures, usually between 1000-1400K^[12-15], depending on the method used. The diamond film can be doped during CVD with the inclusion of other gases into the mix, such as diborane for boron doping^[16] and ammonia for nitrogen doping^[17].

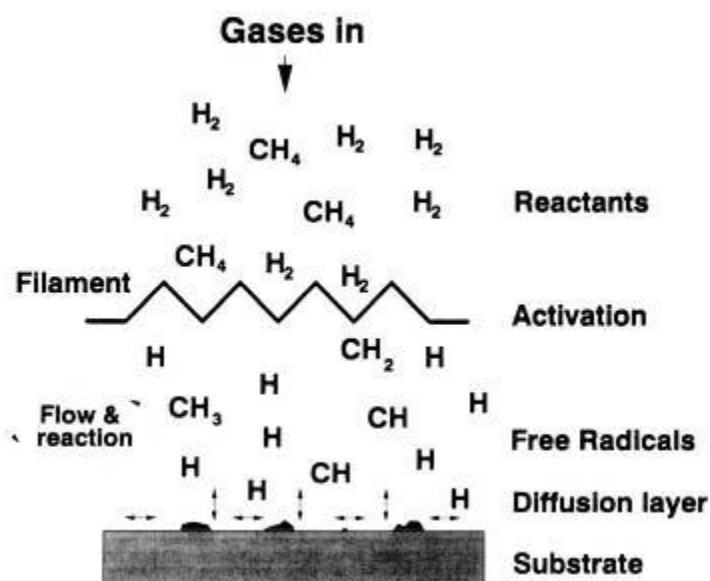


Figure 1.3: The general mechanism for CVD in a hot filament reactor. Gases are activated by the hot filament (or electron bombardment in the plasma for microwave reactors) before diffusing to the substrate surface, forming a diamond film under the correct conditions^[12].

Diamond is not the only allotrope of carbon to be formed during the CVD process, graphite is also formed to a large extent. Graphite is the more stable form of solid carbon at ambient temperatures and pressures, with a large activation barrier between graphite and diamond which prevents simple thermally driven conversion. This would suggest that only graphite would be formed during CVD

rather than diamond, and the reason that diamond is formed is due to the presence of the hydrogen atoms. The atomic hydrogen has several roles; the H-atoms perform an essential role in the activation of methane (producing the methyl radicals required to react with the diamond surface), hydrogen will terminate dangling bonds on the diamond surface to maintain the diamond structure rather than forming sp^2 hybridised carbon and hydrogen radicals will also create active sites on the diamond surface. The molecular H-H bond is stronger than the C-H bonds on the diamond surface, allowing the H-atoms to remove surface-bound hydrogen, creating the vacant site. Due to the excess of hydrogen in the reactor, these vacant sites will most likely be filled by another H-atom, but occasionally they will be filled by a methyl radical, and the diamond surface will grow.

The final role of atomic hydrogen, and the role in which this project is concerned, is the etching of both diamond and graphite. Etching is the removal of the carbon atoms via reactions with gas-phase species and is one of the key mechanistic features of diamond CVD^[18,19]. It is generally accepted that atomic hydrogen etches graphite (sp^2 hybridised carbon) at a significantly higher rate than diamond (sp^3 hybridised carbon), but very little experimental data has been produced to give an exact ratio. Values vary from graphite etching being approximately 20 times faster^[20] to several orders of magnitude faster^[21,22] than that of diamond. Other studies have shown that the graphite and diamond etch rates have different temperature dependencies^[23]. During the CVD growth of diamond the growth rate of diamond is greater than its etch rate, and the opposite is true for graphite (it is etched faster than it grows), this ultimately allows pure diamond to form. Whilst the benefit of graphite etching is obvious, diamond etching is also important for growth. During CVD the diamond can develop a configuration that prevents the growth of a perfect lattice by effectively deactivating certain surface sites. The etching of such configurations allows the surface to be reorganised into a form more favourable for growth^[24].

Etching diamond with atomic hydrogen is itself a useful tool. By exposing a diamond film to hydrogen in a CVD reactor without methane or any other carbon-containing gas, the diamond can be etched without any further growth. For instance, hydrogen plasmas can be used to smooth and polish diamond surfaces^[25]. Previously, surface diffusion on the diamond surface during the growth process was modelled and suggested to be the reason for the production of a smooth diamond surface^[26], but more recent studies show that if surface diffusion was present, diamond growth rates would be higher than those experimentally observed^[27]. This suggests that the smoothing is due to the effects of hydrogen etching.

It is clear that the mechanisms for diamond etching by atomic hydrogen are important in order to fully understand the mechanism of diamond growth, and this will include its affect on the overall rate of growth and the morphology of the surface.

1.3 Etching of Diamond by Atomic Hydrogen

Despite the amount of research that has gone into understanding the growth of diamond films by CVD, the conditions and environments within the reactors are such that direct monitoring of the reactions involved is extremely difficult. Many computational studies have looked into growth on the diamond (100) surface and the various mechanisms involved. These include the initial insertion of

carbon into a reconstructed dimer bond using ring opening/closing mechanisms^[27-30], between dimers via trough bridging mechanisms^[28,31], and mechanisms for the generation of the reconstructed dimer surface^[28]. Other studies have also looked into the migration of CH₂ groups between the (100) and (111) surfaces during growth^[28,32]. Unfortunately the etching of diamond has not been given the same attention and is much less well understood.

Two main conclusions have been drawn regarding the etching of carbon atoms from the diamond surface that help explain many of the phenomenon observed during CVD growth. The first is that atomic hydrogen seems to preferentially etch under-coordinated carbon; carbons that are bound to only two adjacent carbons, rather than three. This explains the presence of large, smooth (100) surface facets on the diamond surface. The second observations is that the diamond surface seems to etch anisotropically, which explains the different relative etch rates of facets with different morphologies, along with various surface features, such as S_A and S_B edges, the smooth, ordered domains and etch pits (*figure 1.4*). As mentioned before, the (100) diamond surface is comprised of dimer rows. The sides of these dimer rows from here on referred to as S_A edges, and edges along the ends of the dimer rows will be referred to as S_B edges, as first denoted by Stallcup *et al*^[33]. S_A and S_B edges are at 90° to each other, and together explain the presence of smooth, ordered rectangular domains on the (100) surface. Double type A steps (D_A) are often observed when the S_B step between two S_A steps is etched right back to the S_A steps. Square pyramidal etch pits also form on the surface under certain conditions, which have triangular facets with the (111) orientation^[34]. These two mechanisms are discussed in turn below.

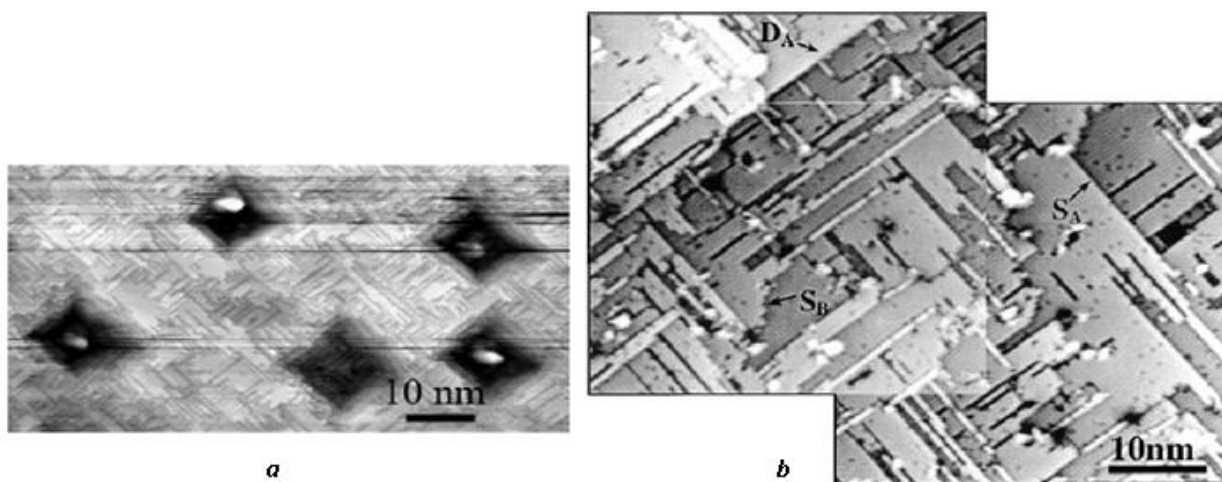


Figure 1.4: (a) STM image of etch pits on a (100) diamond film after exposure to atomic hydrogen for 12 min at 500°C^[35]. (b) STM image of a non-hydrogen terminated diamond (100) surface after atomic hydrogen exposure for 5 min at 1000°C. S_A, S_B and D_A steps, along with some dimer rows, are clearly visible and examples are labelled^[33].

1.3.1 Preferential Etching of Under-Coordinated Carbon

As diamond grows it tends to form either (100) or (111) facets; (100) facets are square shaped, whilst (111) faces are triangular (*figure 1.5*). The (110) faces are rarely observed due to the growth on these faces being significantly higher, with the rate of deposition being almost four times that of the (100) and (111) faces^[36,37]. Many attempts at modelling diamond growth, using chemical kinetic modelling and kinetic Monte Carlo simulations, predict the growth rates of the (100) face to be much higher relative to those on the (110) and (111) observed experimentally^[38-40], and the surface to be rough, rather than smooth^[39,40]. Battaile *et al* showed, using quantum mechanical calculations and atomic-scale kinetic Monte Carlo simulations, that the formation of large, smooth (100) facets can be explained by the preferential etching of under-coordinated carbon atoms on the surface, in the form of CH₂ moieties^[27].

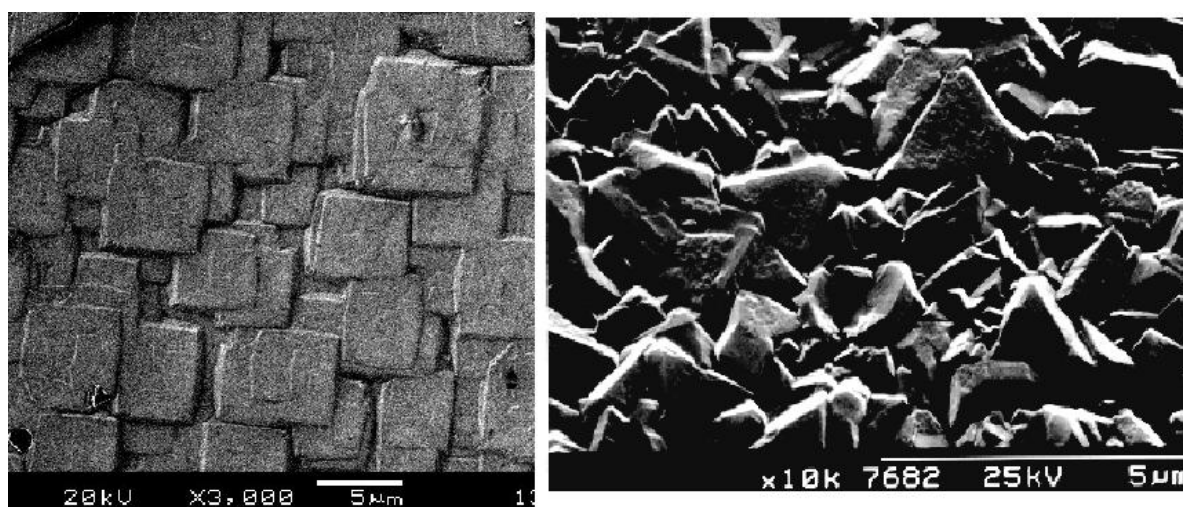


Figure 1.5: SEM images showing square (100) facets and triangular (111) facets on two samples of CVD diamond^[10]

The growth mechanism^[29] (*figure 1.6*) uses a β -scission (*step d*) followed by dimer insertion (*step e*) to incorporate methyl radicals into the (100) surface, the dimer insertion being the rate-limiting step.

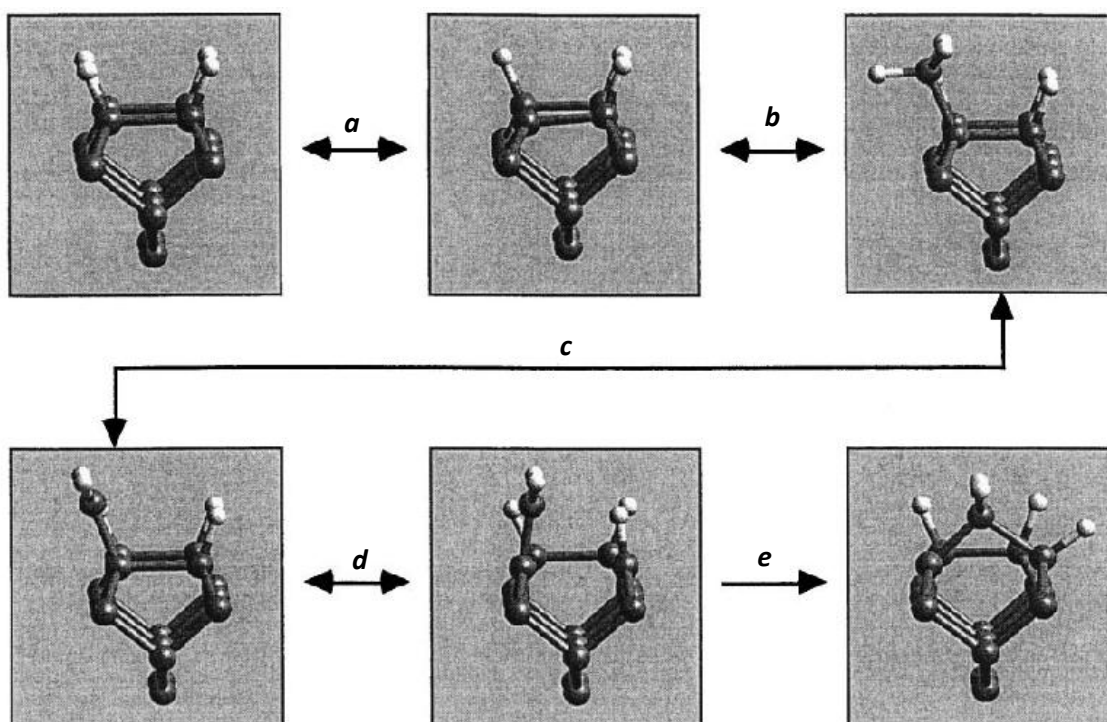


Figure 1.6: The mechanism for the adsorption and incorporation of a methyl radical on a 2×1 (100) diamond surface, leading to growth^[27].

The etching process (figure 1.7) is the reverse of this process, with CH_2 abstracted by atomic hydrogen (step *g*).

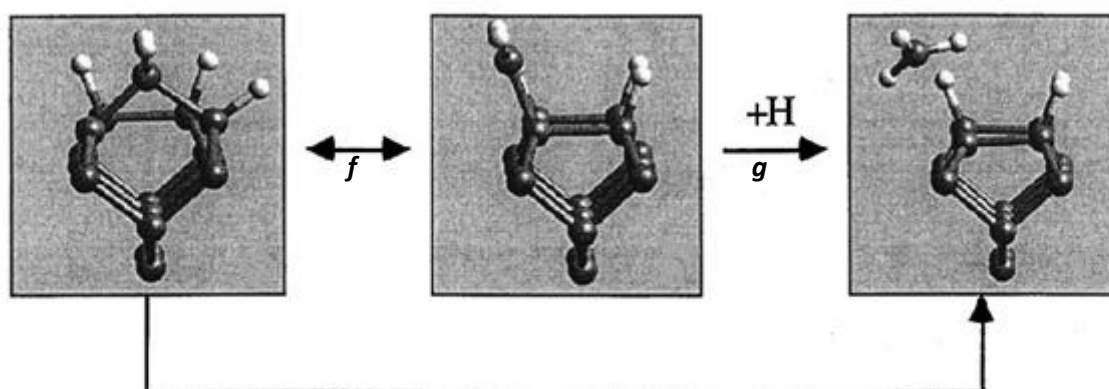


Figure 1.7: The mechanism for the etching of a methyl radical from a diamond 2×1 (100) surface by atomic hydrogen^[27].

Battaile *et al* found that the etching of carbon from the (100) surface occurs at a considerable rate, reducing the overall growth rate to a figure similar to that observed experimentally, whilst not really effecting the (110) and (111) rates, since they contain very few sites that resemble an isolated CH_2 molecule. It was also calculated that the enthalpy change when etching a single carbon atom alone on the surface ($-7.8 \text{ kcal mol}^{-1}$) was significantly lower than when etched from the edge of a S_B step, ($9.4 \text{ kcal mol}^{-1}$) or when etched from within a surface terrace ($57.7 \text{ kcal mol}^{-1}$). This is due to the lattice being constrained when a CH_2 molecule is inserted next to other CH_2 units, which makes it

high in energy, and also due to the higher number of C-C bonds that need to be broken to etch at these sites. Therefore etching is significantly more likely at an isolated carbon on the surface than at a step edge or from within the flat surface. These findings explain the experimentally observed (100) facets, with lone carbons on the surface being etched away, and growth happens parallel to the surface, forming larger (100) faces that will not be etched in this way.

1.3.2 Anisotropic Etching

The preferential etching of under-coordinated carbon does not tell us how ordered (100) domains form, only why they are not etched. Another conclusion, which can explain the formation of smooth (100) and (111) facets, is that the diamond surface etches anisotropically, something that has been observed using spectroscopic techniques such as single-pass Brewster-angle transmission spectroscopy^[41] and scanning tunnelling microscopy^[33]. This anisotropic etching model is based on the theory that a surface will etch at different rates in different directions, compared with isotropic etching, when the probability of removing a surface atom is independent of its coordination resulting in a rough surface^[42].

The etching of (100) surfaces can have slightly varied results depending on the conditions used. Generally, large, smooth (100) domains are formed, with smooth S_A steps and relatively rough S_B steps between them. At high temperatures ($T= 900-1100^\circ\text{C}$) the (100) surfaces are very large^[43] and at very low temperatures ($T= 200^\circ\text{C}$) the surface forms narrow terraces^[43,44]. Within mid ranged temperatures ($T= 500^\circ\text{C}$) etch pits can be observed, which otherwise would only form at dislocations on the surface^[35,45].

Stallcup *et al*^[33] proposed a anisotropic mechanism that explains the formation of large smooth (100) domains with smooth S_A and rough S_B steps. It is also important to understand how the surface grows in this regard. *Figure 1.8* shows a schematic diagram of the diamond 2×1 (100) surface. As we have already discussed, growth on this diamond surface occurs when methyl radicals are adsorbed and form methylene bridges and dimers, which in turn extends the dimer rows. If a methyl radical has adsorbed onto a dimer bond to the right of a growing dimer row, it can prevent further growth of the dimer row due to steric repulsion. For instance, if a methyl radical adsorbs and forms a methylene bridge between atoms **3** and **4**, the steric bulk of this new bridge will prevent another methyl radical adsorbing between atoms **1** and **3**. This would prevent further growth until the methylene bridge between **3** and **4** is etched. Lone dimers forming on S_A steps, such as one that could form between **3** and **4** or at atoms **5** and **6** are kinetically unstable to etching, as are dimers at the end of dimer rows. Dimers within a dimer row that aren't at the end of the S_A row are stable, however, and so atoms **7** and **8** for example will only be etched after atoms **9** and **10** have been removed. Overall this means that although growth can happen at any location, preferential etching means that the dimers will form at S_B steps, extending the dimer rows in a smooth (100) monolayer. Under purely etching conditions (i.e. in the absence of carbon species) these monolayers will be etched at the S_B steps, which result in a rough S_B rows. S_A rows are fairly unaffected so they appear as smooth straight lines. It is energetically much harder to remove a dimer from within the smooth (100) surface, so the rate of etching the S_B rows parallel to the diamond film is significantly faster than the perpendicular etch rate, with etching ratios in the range of 10:1^[34] to 70:1^[25].

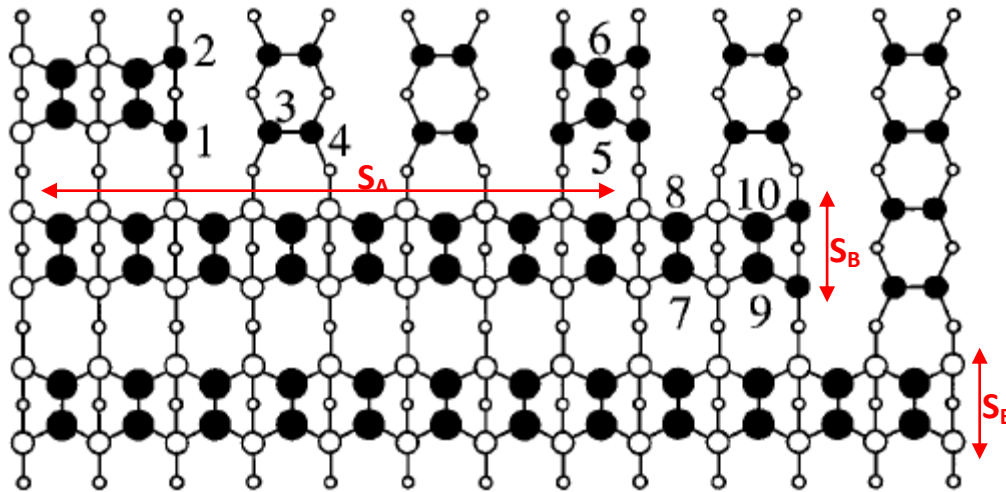


Figure 1.8: A schematic diagram of the top-down view of a 2×1 (100) diamond surface. The large, middle and small sized circles represent carbon atoms in the top, second and third layers respectively. Shaded circles represent carbon atoms which are hydrogen terminated. S_A steps run parallel to dimer rows, whilst S_B steps run perpendicular to them^[33].

Stallcup *et al*^[34] proposed that dimer etching can be caused by the formation of dihydrides on the surface, and that this particular method of etching is responsible for the formation of etch pits. The C-C backbonds of dihydrides on the surface are highly strained due to the steric repulsion of the dihydride units, and are thus susceptible to etching, this is one of the reasons that dimers at steps are more susceptible to etching as they can more easily accommodate dihydride formation^[3]. At mid-range CVD temperatures, around 500°C, atomic hydrogen forms localized regions of dihydrides on the diamond surface. The large amount of stress allows dimers to be etched, forming a defect in the previously smooth surface. Lateral etching of the dimer rows can then take place, forming square pits. The rate of etching perpendicular to the surface is high enough that the steps form triangular (111) surfaces. This is not observed at lower temperatures (~200°C), as there is not enough energy to overcome the dihydride formation activation energy, and at higher temperatures (~1000°C) it is not seen because the C-H bond is less stable with respect to the C-C bond, so monohydride formation is more energetically favourable^[34]. The number of etch pits that can form on a single surface seems to be limited. This is believed to be caused by the diffusion of the hydrogen and hydrocarbon species across the surface, preferentially sticking to the steps on the already formed etch pits and etching there, expanding the existing pit rather than adsorbing to the (100) surface and forming a new etch pit^[34].

Over longer etch periods, Cheng *et al* found that etching on both (100) and (110) surfaces irreversibly formed (111)-orientated facets, whereas (111) surfaces remained relatively unchanged^[41]. The (100) surface is easier to etch relative to the (111) surface because each surface carbon has one of its C-C backbonds lying parallel to the crystal surface, making it readily accessible to atomic hydrogen. Once insertion has occurred, the new C-H bond will twist away from the surface to reduce the bond strain, stabilising the hydride intermediate, which will go on to release CH₄. Similarly, each surface carbon on the (110) surface has two C-C backbonds parallel to the crystal surface. Cheng's data, using infrared techniques, shows the formation of (111) facets on (100) surfaces, and the formation of both (111) and a small amount of (100) facets on (110) surfaces (figure 1.9).

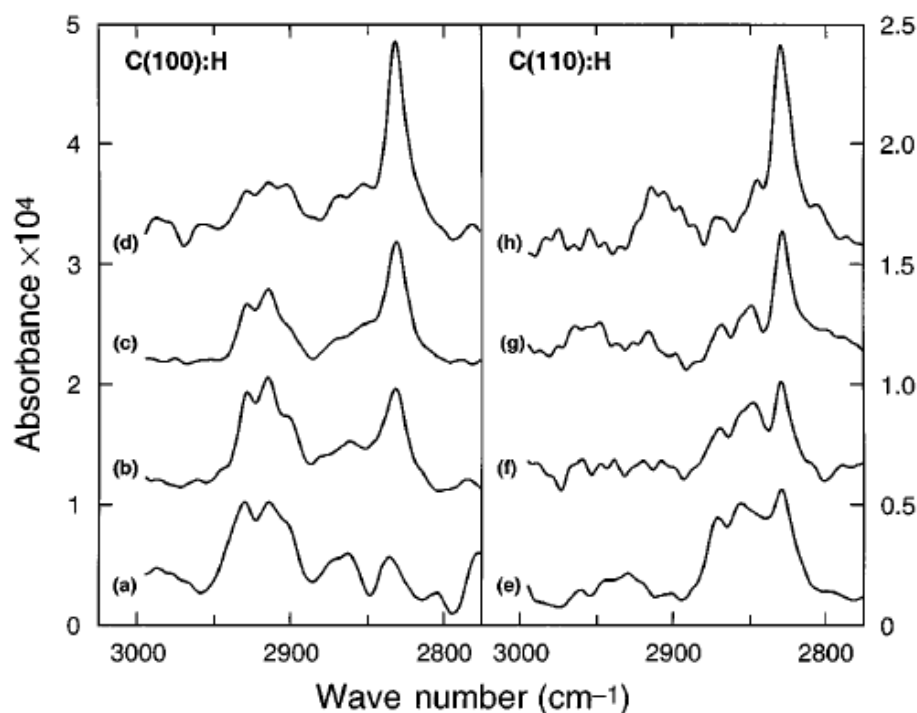


Figure 1.9: The infrared spectra of C-H stretches as a function of hydrogen etching time of 3,4,5 and 8h (a-d) for the (100) surface and 3,7,8 and 9h (e-h) for the (110) surface. C-H stretches in the 2920 cm^{-1} range can be assigned to (100) facets, the singlet peak at 2830 cm^{-1} assigned to (111) facets, and the signal at 2850-2870 cm^{-1} assigned to (110) facets^[41].

1.4 Aim of the Study

This study has taken a detailed look into the etching of diamond within a hydrogen plasma in a microwave reactor. As previously mentioned, this topic has been quite widely researched already, but there is a fair amount of variation in some of the key rates of etching and mechanisms described. The main aim of this study was to investigate these rates of etching, to find values for the relative etch rates of diamond and graphite and to obtain a ratio of the etch rates both parallel to and vertical to the 2×1 (100) reconstructed diamond surface. The conditions used were as close to CVD conditions as possible with the notable absence of methane to prevent any growth.

The diamond and graphite etch rates were studied using PCD samples, and pure graphite samples. The etch rates were calculated as a mass loss over a time period, with the surface area of the samples taken into account. The vertical and parallel etch rates were compared using SCD samples, analysing surface roughness and the dimensions of etch pits formed by atomic force microscopy (AFM) in order to find the etch rate ratio.

Finally, a mechanism for the etching of a dimer from the (100) surface was proposed. It was analysed using computational techniques, looking at the energetics of processes such as the abstraction and adsorption of hydrogen on the reconstructed surface and the transition states involved in these reactions with the surface.

1.5 References

- [1] Drory, M.D., Gardinier, C.F., Speck, J.S. *J Am Chem*, 74 (1991), 3148
- [2] Chong, K.F., PhD thesis, National University of Singapore, 2009 'Development of biosensor and electrochemical studies of carbon-based materials', available from:
<http://scholarbank.nus.edu.sg/bitstream/handle/10635/17738/ChongKF.pdf?sequence=1>
- [3] King, J. 3rd year library project, University of Bristol, 2012 'Growth of cells on CVD diamond surfaces', available from <http://www.chm.bris.ac.uk/pt/diamond/>
- [4] Prelas, M. A., Popovici, G., Bigelow, L. K., *Handbook of Industrial Diamonds and Diamond Films*, Marcel Dekker Inc, 1998.
- [5] Wilkes J., Wilks E.M., *J.E. Field (ed), The Properties of Diamond*, Academic Press, 1979, 352
- [6] Field J.E., *J.E. Field (ed), The Properties of Diamond*, Academic Press, 1979, 284
- [7] Tsuno, T., Tomikawa, T., Shikata, S., Imai, T., Fujimori, N. *Appl. Phys. Lett.* 64 (1994), 572
- [8] Nützenadel, C., Küttel, O. M., Diederich, L., Maillard-Schaller, E., Gröning, O., Schlapbach, L. *Surf. Sci.* 396 (1996), L111
- [9] Bobrov, K., Mayne, A., Comtet, G., Dujardin, G., Hellner, L., Hoffman, A. *Phys. Rev. B.* 68 (2003), 195416
- [10] <http://www.chm.bris.ac.uk/pt/diamond/>
- [11] Hall, H.T., *Science*, 128 (1958), 445
- [12] Ashfold M.N.R., May P.W., Rego C.A., Everitt N.M., *Chem. Soc. Rev.*, 23 (1994) 21
- [13] Brunet, F., Germi, P., Pernet, M., Deneuille, A., Gheeraert, E., Mambou, J., *Diam. Rel. Mater.*, 6 (1997), 774
- [14] Yan, C.S., Mao, H.K., Li, W., Qian, J., Zhao, Y., Hemley, R.J., *Phys. Status Solidi A*, 201 (2004), R25
- [15] Bogdan, G., Nesládek, M., DiHaen, J., Maes, J., Moshchalkov, V.V., Haenen, K., D'Olieslaeger, M., *Phys. Status Solidi A*, 202 (2005), 2066.
- [16] Luong, J.H., Male, K.B., Glennon, J.D. *Analyst*, 134, 10, (2009), 1965
- [17] May P.W., Burridge P.R., Rego C.A., Tsang R.S., Ashfold M.N.R., Rosser K.N., Tanner R.E., Cherns D., Vincent R., *Diamond Rel. Mater.* 5 (1996) 354
- [18] Fedosayev D.V., Deryagin B.V., Varasavskaja I.G., *Surf. Coat. Technol.* 38 (1989), 9
- [19] Spitsyn B.V., Bouilov L.L., Derjaguin B.V., *J. Cryst. Growth.* 52 (1981), 219

- [20] Bachmann P.K., *Adv. Mater.* 2 (1990) 195
- [21] Deryaguin B.V., Fedoseev, D.V., *Izd Nauka, Moscow*, 1997
- [22] Setaka N., *J. Mater. Res*, 4 (1989) 664
- [23] Donnelly C.M., *et al. Diamond and Relative Materials*, 6 (1997), 787
- [24] Netto A., Frenklach, M., *Diamond and Related Materials*, 14, 10 (2005), 1630
- [25] Gaisinskaya A., Edrei R., Hoffman A., Feldheim Y., *Diamond and Relative Materials*, 18 (2009), 1466
- [26] Frenklach M., Skokov S., *J. Phys. Chem. B*, 101 (1997), 3025
- [27] Battaile C.C. *et al, J. Chem. Phys*, 111 (1999), 4291
- [28] Cheesman, A., Harvey, J.N., Ashfold, M.N.R., *J. Phys. Chem. A.*, 112 (2008), 11436
- [29] Garrison B.J., Dawnkaski E.J., Srivastava D., Brenner D.W., *Science* 255 (1992), 835
- [30] Oleinik, I.I., Pettifor, D.G., Sutton, A.P., Butler, J.E., *Diam. Rel. Mater.*, 9 (2000), 241
- [31] Harris, S.J., *Appl. Phys. Lett.*, 56 (1990), 2298
- [32] Richley, J.C., Harvey, J.N., Ashfold, M.N.R., *J. Phys. Chem. C*, 116 (2012), 7810
- [33] Stallcup R.E., Perez J.M., *Physical Review Letters*, 86 (2001), 15
- [34] Stallcup R.E., Mo Y., Scharf T.W., Perez J.M., *Diamond and Relative Materials*, 16 (2007), 1727
- [35] Jiang X., Rickers C., *Appl. Phys. Lett.* 75 (1999) 3935
- [36] Spear, K. E. *J. Am. Ceram. Soc.* 72 (1989), 171
- [37] Chu C.J., Hauge R.H., Margrave J.L., D'Evelyn M.P., *Appl. Phys. Lett.* 61 (1992), 1393
- [38] Harris S.J., Goodwin D.G., *J. Phys. Chem.* 97 (1993), 23
- [39] Dawnkaski E.J., Srivastava D., Garrison B.J., *J. Chem. Phys.* 104 (1996), 5997
- [40] Battaile C.C., Srolovitz D.J., Butler J.E., *J. Cryst. Growth*, 194 (1998), 353
- [41] Cheng C.L., Chang H.C., Lin J.C., Song K.J., *Physical Review Letters*, 78 (1997), 19
- [42] Boland, J., *Surf. Sci.*, 17 (1992), 262
- [43] Stallcup R.E., Perez J.M., *Appl. Phys. Lett.*, 81 (2002), 4538
- [44] Stallcup R.E., Ph.D. dissertation, University of North Texas (2000)
- [45] Mitsuhashi M., Karasawa S., Ohya S., Togashi F., *Appl. Surf. Sci.* 60/61 (1992) 565

Chapter 2 – Experimental

2.1 The Microwave Reactor

The microwave (MW) reactor system is based on an ASTeX design, with a process chamber purpose built and donated by Element Six Ltd. The plasma reactor consists of a vertically aligned aluminium cylinder (height = 175mm, internal diameter = 120mm) which is cooled by a constant flow of water. Sample substrates are placed on a Mo holder, which is kept separate from the water-cooled Al baseplate by a 250- μm -thick W wire ring which acts as a thermal break. The reactor chamber is divided into two by a quartz window, with the low-pressure plasma reactor below and the MW waveguide above. The quartz window is cooled by a blower, passing a stream of air across its upper surface. The pressure within the chamber is maintained with a butterfly valve, throttling the exhaust from the chamber, which works using a feedback from the chamber pressure gauge. Working pressures and the base pressure are measured using a 1000 Torr capacitance manometer and a Pirani gauge respectively. A two-stage rotary pump (Edwards E2M8) is used to create a high vacuum (10^{-3} Torr). Substrate temperature is measured using a two-wavelength optical pyrometer (Raytek Thermalert SX) positioned above the reactor, focused onto the substrate. The microwave radiation responsible for the activation of the gas mixture are generated at 2.45 GHz by a 1.5 kW ASTeX magnetron (HS-1000).

The gas mix ratios are controlled electronically with an array of mass flow controllers. The gases are mixed into one $\frac{1}{4}$ " pipe which splits and enters the reactor chamber from opposite sides, just below the quartz window. The gas mixture used consists of pure H_2 with a flow rate of 500 standard $\text{cm}^3 \text{min}^{-1}$ (sccm).

The reactor set-up allows the total control of gas composition, pressure and MW power. Stable operating pressures vary from around 40 to 200 Torr, and the MW power can reach around 1.5 kW before the heating of the magnetron by reflected power becomes a problem. Substrate temperature cannot be directly controlled, being a function of the other three controllable variables.

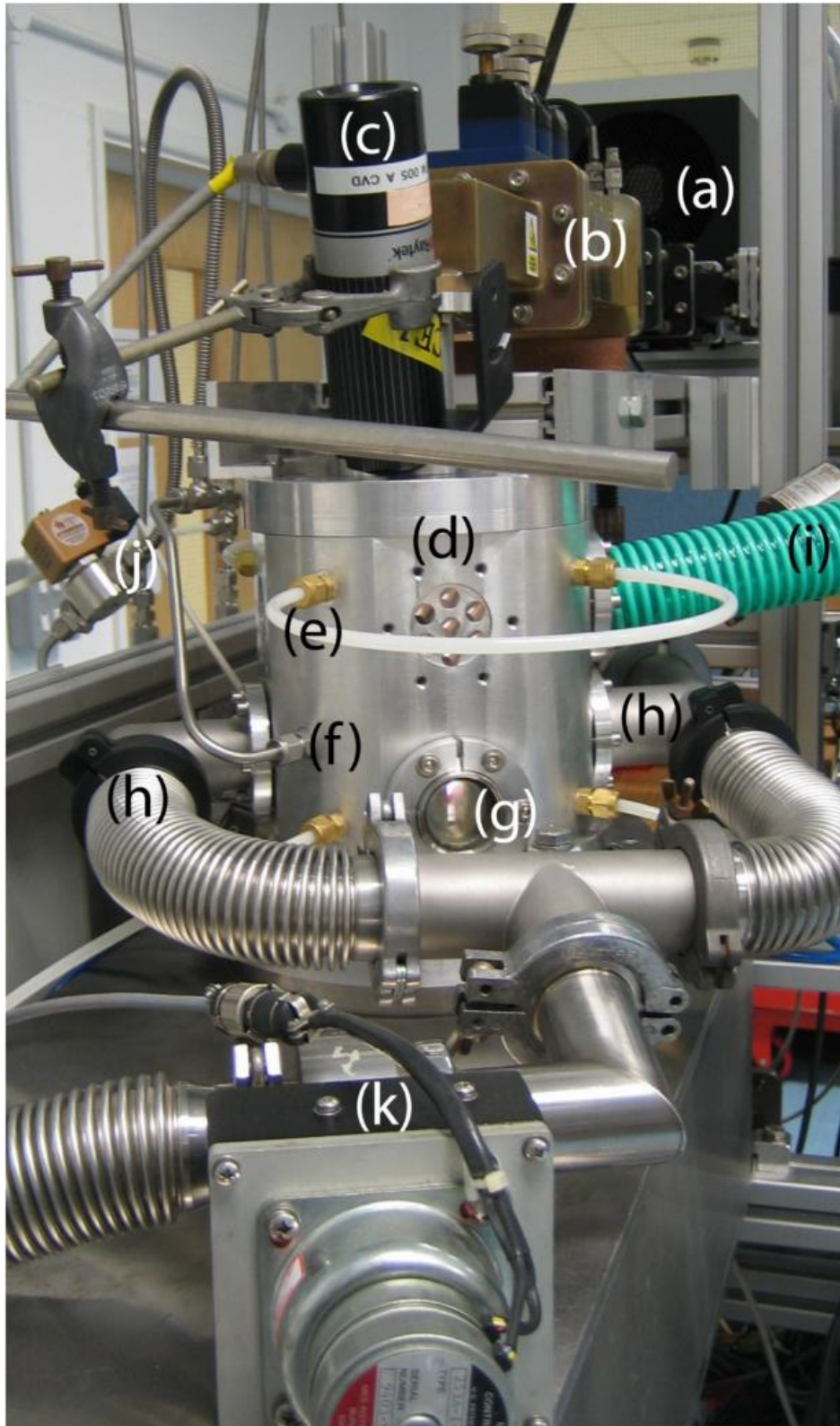


Figure 2.1: The MWCVD apparatus used for diamond etching^[1].
Labelled parts: (a) MW magnetron, (b) MW waveguide, (c) optical pyrometer, (d) reactor chamber, (e) water cooling circulation pipes, (f) process gas inlet, (g) viewing window, (h) gas exhaust, (i) air cooling pipe, (j) solenoid valve, (k) pressure regulating butterfly valve.

2.2 Atomic Force Microscopy

Atomic force microscopy (AFM) was used to analyse and map out the surface topography of the SCD samples before and after etching, allowing for the accurate measuring of etch pit dimensions at nanometre resolution. AFM raster a silicon nitride probe (radius < 10nm) attached to a cantilever across the sample surface. As the probe scans the surface it is deflected slightly by topography of the surface, in accordance to Hooke's Law. The magnitude of the deflection depends on the magnitude of the surface feature the probe is scanning across. A laser, aligned with the tip of the cantilever, reflects off the cantilever at an angle determined by the magnitude of deflection, and is used to create an image of the sample surface. The AFM equipment was comprised of a Bruker Multimode AFM instrument combined with a Nanoscope V controller. Tapping mode, in which the probe literally taps across the surface rather than being in constant contact, was used to reduce cantilever wear, which can become a problem with hard surfaces such as diamond^[2]. Images were analysed using Nanotech Electronica WSxM software^[3].

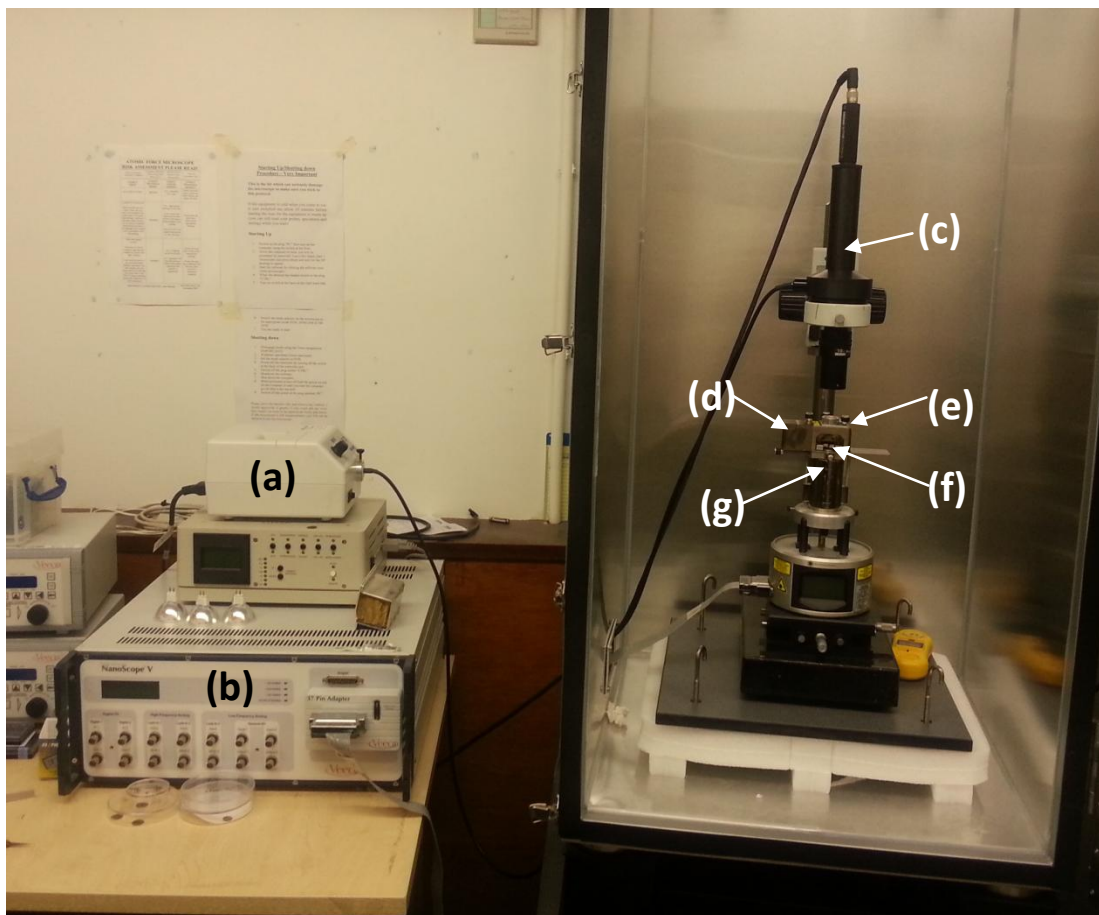


Figure 2.2: The AFM apparatus used for surface characterisation.

Labelled parts: (a) Light source, (b) Control box, (c) Microscope, (d) Laser source, (e) Cantilever head, (f) Cantilever, (g) Sample stage.

2.3 Diamond and Graphite Etch Rate Comparison

Polycrystalline diamond (PCD) samples, purchased from Element Six Ltd, were grown by CVD and mechanically polished to a thickness of 0.25mm, then cut into 1.0 x 1.0 cm squares. The diamond samples were cleaned by refluxing in aqua regia, formed by adding KNO₃ (6.5g) to H₂SO₄ (100ml), for 15 minutes. Graphite disks were cut from a graphite rod to create samples 0.3 mm thick with a diameter of 1.0 cm. Sample mass was recorded to the nearest microgram. Hydrogen gas flow (F) and microwave power (P) were kept constant, the pressure (p) was varied, and the temperature (T) was measured using the optical pyrometer. The etch time (t) differed for diamond and graphite due to the large expected difference in etch rate. *Table 2.1* shows the process conditions for each run.

Sample	A / cm^2	P / kW	F / sccm	p / Torr	t	$T / ^\circ\text{C}$
PCD-A	1	1	500	150	6 hr	695
PCD-B	1	1	500	100	6 hr	670
Graphite-A	0.79	1	500	100	40 min	670

Table 2.1: Etch conditions P , F , p , t , T , and the sample surface area A for PCD samples A and B, and Graphite sample A.

2.4 Lateral and Vertical Etch Rate Comparison

Single crystal (100) diamond (SCD) films, purchased from Element Six Ltd, were grown by CVD and mechanically polished to a thickness of 0.5 mm, then cut into 3.0 x 3.0 mm squares. In order to increase the number of samples available two of the SCD films were cut in half using an Oxford Laser Micro-Machining System to give four 3.0 x 1.5 mm samples. Samples were cleaned by refluxing in aqua regia for 15 minutes. Hydrogen gas flow (F) and microwave power (P) were kept constant, the pressure (p) and etch time (t) were varied, and the temperature (T) was measured using the optical pyrometer. *Table 2.2* shows the process conditions for each run. Samples were analysed before and after treatment by AFM.

Sample	d / mm	P / kW	F / sccm	p / Torr	t / min	$T / ^\circ\text{C}$
1	3.0 x 3.0 x 0.3	1.0	500	100	30	560
2	3.0 x 3.0 x 0.3	1.0	500	125	30	560
3	3.0 x 3.0 x 0.3	1.0	500	150	30	660
4	3.0 x 1.5 x 0.3	1.0	500	100	25	545
5	3.0 x 1.5 x 0.3	1.0	500	125	25	560
6	3.0 x 1.5 x 0.3	1.0	500	150	25	570

Table 2.2: Etch conditions P , F , p , t , T , and the sample dimensions d for samples A-G.

2.5 Computational Studies into the Mechanism of Etching

The proposed mechanism was investigated using two techniques with a smaller $C_{17}H_{22}$ cluster (figure 2.3) and a larger $C_{97}H_{74}$ cluster (figure 2.4) to replicate part of a H terminated, 2×1 (100) reconstructed diamond surface. In order to see if the mechanism was realistic and worth further investigation, quick semi-empirical calculations at PM3 level on the Gaussian03 program^[4] were used. These gave the potential energy minima and transition states (TSs) associated with the interaction between atomic hydrogen and both the $C_{17}H_{22}$ and $C_{97}H_{74}$ clusters and the optimized C-C and C-H bond lengths. Vibrational frequencies were also calculated to confirm the nature of stationary points and to obtain estimates for the zero-point energy correction. Having proven the eligibility of the mechanism, the process was repeated using a more accurate density functional theory (DFT) method with the $C_{17}H_{22}$ cluster as the larger cluster proved to be too computationally demanding for this project. Using the B3LYP functional and the 6-31G(d) basis set structures were fully optimized, vibrational frequencies were again calculated as before.

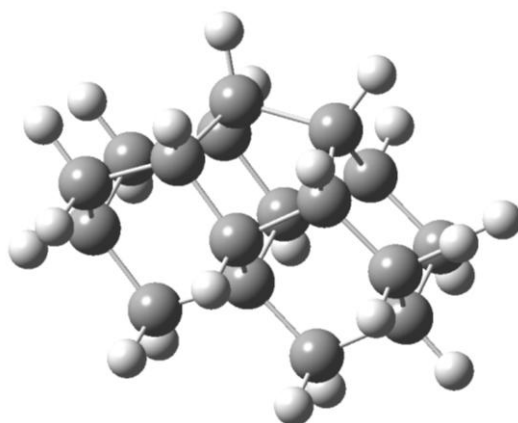


Figure 2.3: A ball and stick representation of the $C_{17}H_{22}$ cluster used to model the H-terminated, 2×1 (100) reconstructed diamond surface.

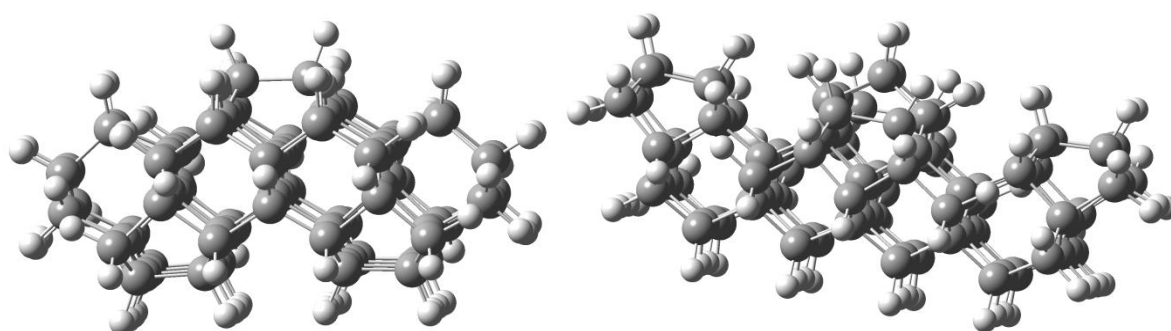


Figure 2.4: A ball and stick representation of the $C_{97}H_{74}$ cluster used to model the H-terminated, 2×1 (100) reconstructed diamond surface. The two images are at 90° to each other, clearly showing the lone carbon dimer on the top, and the dimer rows of the layer below.

2.6 References

[1] Fox, O., PhD thesis, August 2011 "Deposition of nanocrystalline diamond films by MW plasma CVD and Gas-phase diagnostics using *in-situ* molecular-beam mass spectrometry and emission spectroscopy" available from <http://www.chm.bris.ac.uk/pt/diamond/>

[2] Achatz, P., Garrido, J. A., Williams, O. A., Brun, P., Gruen, D. M., Kromka, A., Steinmüller, D., Stutzmann, M., *Physica Status Solidi*, 204(9) (2007), 2874.

[3] Fernandez, H.R., Gomez-Rodrigues, J.M., Cochero, J., Gomez-Herrero, J., Baro, A.M., *Rev. Sci. Instrum.* 78 (2007), 13705

[4] Frisch, M. J., Trucks, G. W., Schlegel, H. B., Scuseria, G. E., Robb, M. A., Cheeseman, J. R., Montgomery, J. A., Jr., Vreven, T., Kudin, K. N., Burant, J. C., Millam, J. M., Iyengar, S. S., Tomasi, J., Barone, V., Mennucci, B., Cossi, M., Scalmani, G., Rega, N., Petersson, G. A., Nakatsuji, H., Hada, M., Ehara, M., Toyota, K., Fukuda, R., Hasegawa, J., Ishida, M., Nakajima, T., Honda, Y., Kitao, O., Nakai, H., Klene, M., Li, X., Knox, J. E., Hratchian, H. P., Cross, J. B., Adamo, C., Jaramillo, J., Gomperts, R., Stratmann, R. E., Yazyev, O., Austin, A. J., Cammi, R., Pomelli, C., Ochterski, J. W., Ayala, P. Y., Morokuma, K., Voth, G. A., Salvador, P., Dannenberg, J. J., Zakrzewski, V. G., Dapprich, S., Daniels, A. D., Strain, M. C., Farkas, O., Malick, D. K., Rabuck, A. D., Raghavachari, K., Foresman, J. B., Ortiz, J. V., Cui, Q., Baboul, A. G., Clifford, S., Cioslowski, J., Stefanov, B. B., Liu, G., Liashenko, A., Piskorz, P., Komaromi, I., Martin, R. L., Fox, D. J., Keith, T., Al-Laham, M. A., Peng, C. Y., Nanayakkara, A., Challacombe, M., Gill, P. M. W., Johnson, B., Chen, W., Wong, M. W., Gonzalez C., Pople, J. A. *Gaussian 03*, revision B.04, Gaussian, Inc.: Pittsburgh PA, 2003.

Chapter 3 – Results and Discussion

3.1 Diamond and Graphite Etch Rate Comparison

Finding the ratio of graphite and diamond etch rates over the range of conditions under which CVD diamond growth can occur is of great importance when trying to fully understand diamond growth, and in creating a comprehensive growth model. The aim of the investigation was to find the relative rates of mass loss over a period of time using a wide range of etching conditions starting by varying the pressure, which could then be followed by varying other conditions such as power. Diamond samples were etched for significantly longer than the graphite samples to obtain a measurable mass loss.

Etching the graphite samples soon became problematic. The samples were too light and under some conditions the plasma would be pushed under the substrate, causing the sample to flip off the sample stage and out of the plasma, terminating the etching experiment. To resolve this, a special sample stage was ordered with a milled recess. The sample would fit into the recess, preventing the plasma from getting beneath the sample and displacing it from the sample stage. Unfortunately the sample stage was not prepared in time to be used within the time constraints of this project.

Sample	p / Torr	Mass Loss /mg	Mass Loss Rate / $\text{mg hr}^{-1} \text{cm}^{-2}$
PCD-B	150	1.134	0.189
PCD-C	100	0.465	0.0775
Graphite-A	100	8.112	15.403

Table 3.1: The rate of mass loss per unit area for the three successful runs, along with the pressures they were run at. Other run conditions can be seen in Table 2.1.

The preliminary results give a rough graphite : diamond etch rate ratio of 200:1 at pressures of 100 Torr. Whilst this is a good first approximation, it does not necessarily hold true under different conditions, and further work is required to fully comprehend how the etch rate ratios vary as reactor pressure and microwave power are changed.

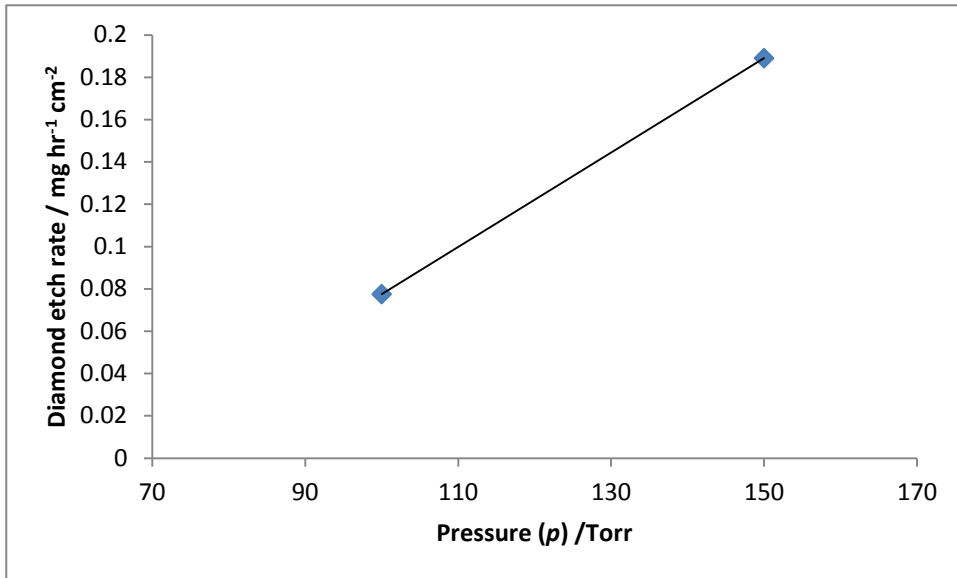


Figure 3.1: Plot of diamond etch rate per unit area as a function of reactor pressure (p).

The plot of diamond etch rate as a function of reactor pressure (*figure 3.1*) gives the following equation for the etch rate:

$$\text{Etch Rate} = 0.0022p - 0.1455 \quad (1)$$

This does not truly represent the dependence of the diamond etch rate upon pressure since only two pressures were successfully used to obtain etch rates. Previous studies have found that the both diamond and graphite etch rates have non-linear relationships with temperature^[1], and as temperature is dependent on both the power and pressure used, it is impossible to rule out the possibility that the etch rates also have a non-linear relationship with reactor pressure and microwave power. As such it is necessary to expand the range of conditions used, when the new sample stage is available, in order to determine the true relationships.

3.2 Lateral and Vertical Etch Rate Comparison

Whilst it is widely accepted that a diamond (100) surface etches parallel to the surface faster than it etches perpendicular to the surface (diamond etches anisotropically), a more thorough investigation into the ratio of these etch rates is required to model diamond growth more accurately.

Investigating the etch rate ratio posed a unique problem in that it needs an identifiable point from which both vertical and lateral etching began in order for the two to be compared. This problem was addressed by analysing pyramidal etch pits on the surface, and assuming that the centre of the etch pit was the etching starting point. The main disadvantage of using etch pits however is that they only appear over a relatively narrow range of CVD conditions; if the lateral and vertical etch rate ratio changes over the wider range of CVD conditions, studying etch pits will not give a full description of how the etch rates vary. Previous studies have shown that etch pits tend to form over the mid-ranges of temperature, around 500°C^[2,3]. The reactor temperature could not be directly controlled,

however for the pressures and power we were interested in the temperature was close enough, at around 600°C. The pressure and time were varied for a total of six runs (*Table 2.2*).

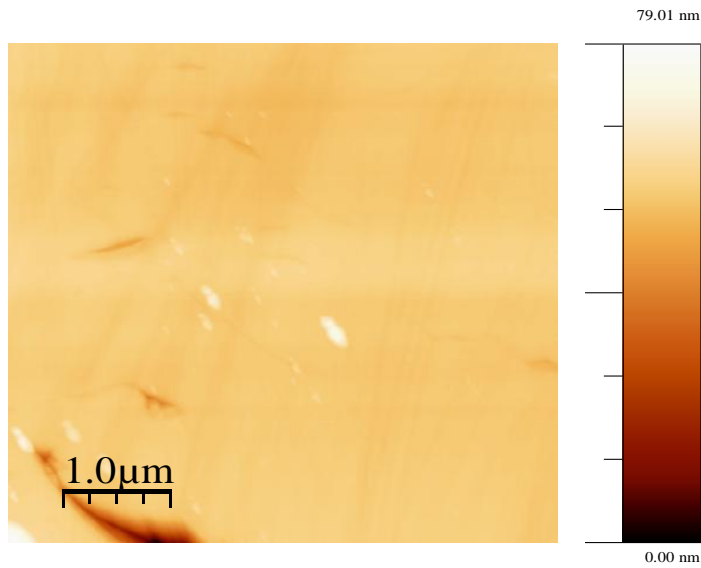


Figure 3.2: A pre-etch AFM image of a polished SCD sample. The average surface roughness is 1.3442 nm. Mechanical polishing scratch lines can be seen across the surface, along with the some small surface defect.

Sample 1 (*figure 3.3*) showed roughly uniform square etch pits dotted all over the surface, and clustered around scratches and deformities that were present prior to etching. Whilst it was possible to make out etch pits around the deformities, they were so densely packed that measuring their dimensions was difficult. As such only the lone etch pits were counted and measured. Surface deformities expose the ends of dimer rows, allowing rapid lateral etching, which leads to square etch pit-like features clustered around the deformity, something that was observed on all samples, with or without etch pits. For an etch pit to form on a smooth surface, a dimer from within a dimer row must first be removed, which theoretically is almost impossible and is the reason etch pits only form in such a narrow range of conditions.

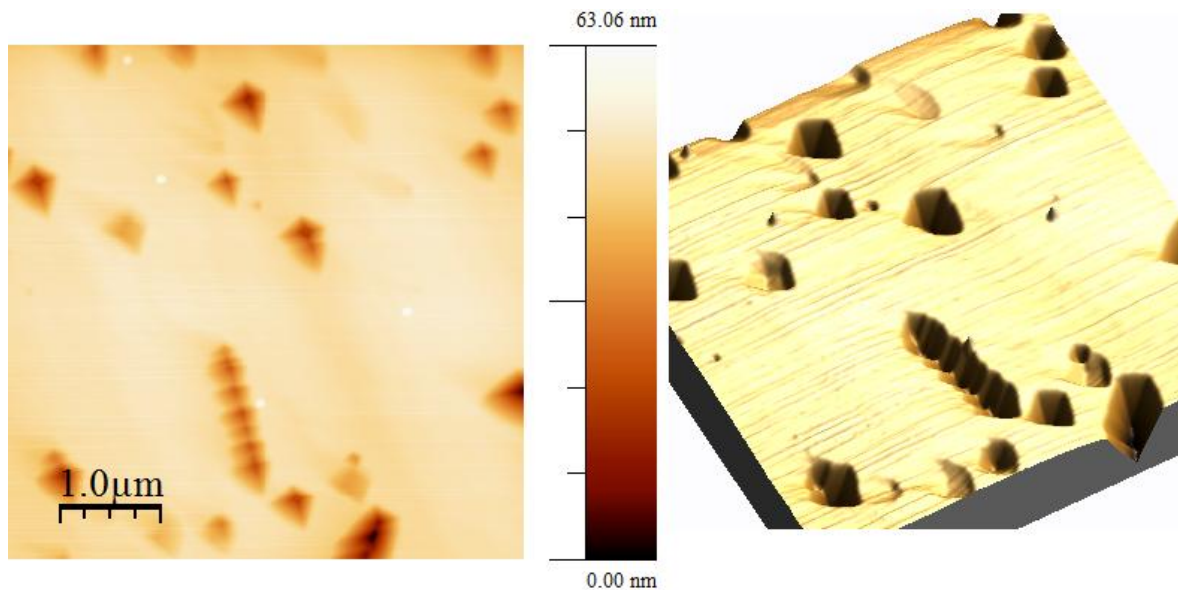


Figure 3.3: A $5 \times 5 \mu\text{m}$ AFM picture of sample **1** post-etch, in 2D and 3D. The picture shows many square etch pits of roughly the same size.

Sample **2** (figure 3.4) showed smooth regions surrounded by large step edges, roughly running in the same direction to each other. This shows the diamond surface during the process of smoothing, as entire layers of diamond are etched away laterally until, theoretically, there are no remaining surface defects and the surface is perfectly smooth. As etch pits grow, etching away at the diamond (111) surfaces that form the triangular facets of the etch pit, they will eventually expand into other etch pits. The (111) facets of etch pits, when viewed from a (100) perspective, are simply a series of D_A layers and when two etch pits collide, the S_B ends of these rows are exposed, leading to rapid lateral etching, significantly faster than the usual etching of the (111) facets. This will eventually result in the large straight D_A and rougher S_B step edges seen on sample **2**. Square, etch pit-like features could still be observed around the deeper surface defects, but these could not be measured to give any useable data without detailed knowledge of the defect geometries prior to etching

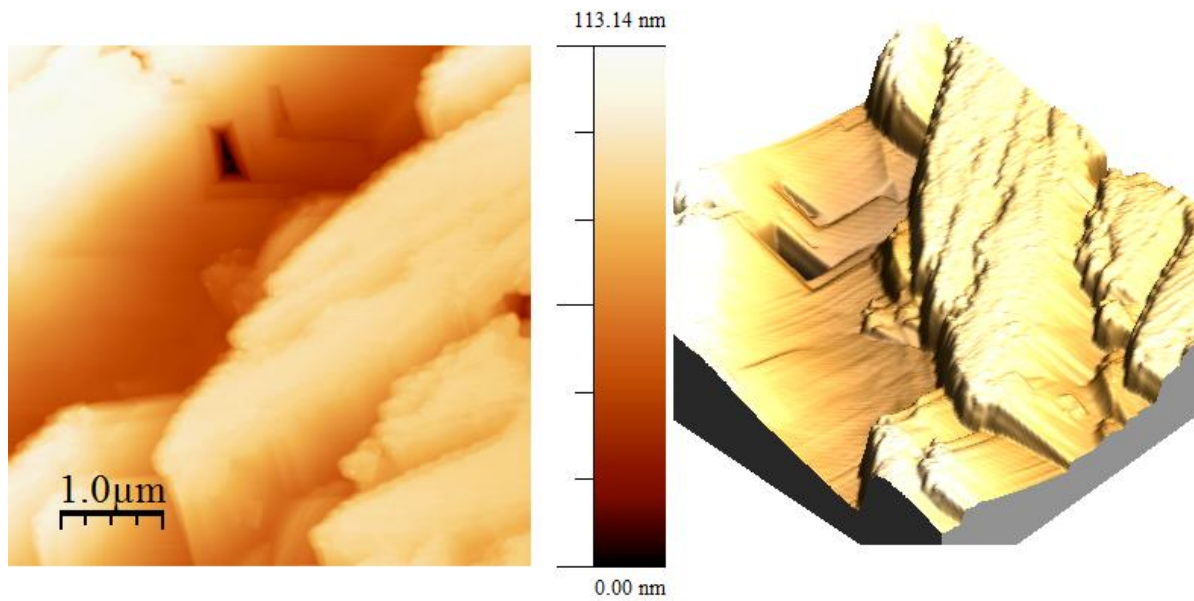


Figure 3.4: A $5 \times 5 \mu\text{m}$ AFM picture of sample **2** post-etch, in 2D and 3D. Large steps can be seen, being etched away to leave a smoother surface. The straight sides to the steps are D_A steps, whilst the rougher sides are a series of S_B edges.

The surface of sample **3** (figure 3.5) was very smooth with no terraces and square, etch pit-like features clustered around the remaining surface defects. This suggests that the lateral etching of entire layers, as observed in sample **2**, has finished which leaves the surface smooth. Only the deepest defects from the original surface remain. It can also be observed that some very small etch pits exist on some of the AFM images, these are most likely to be new etch pits that had just begun to form on the new smooth surface.

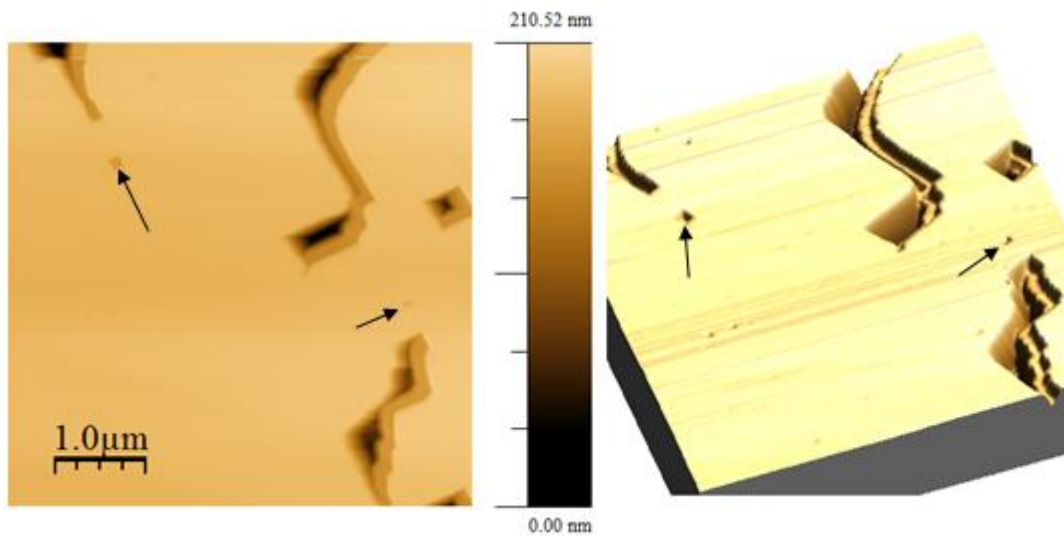


Figure 3.5: A $5 \times 5 \mu\text{m}$ AFM picture of sample **3** post-etch, in 2D and 3D. Samples of the small etch pits are highlighted with arrows.

The initial intention was to only vary the pressure, but having analysed the first three samples it was decided that it would be better to run the remaining samples at the same pressures but for less time, in order to try and observe any etch pits formed prior to the smoothing observed in **2** and **3**.

Sample **4** (figure 3.6) showed no sign of etch pits, and the usual square features clustered around the surface defects were relatively small compared to previous samples. Etch pits had not yet had time to grow, suggesting that the etch pits observed on sample **1** were formed between 25 and 30 minutes of etching.

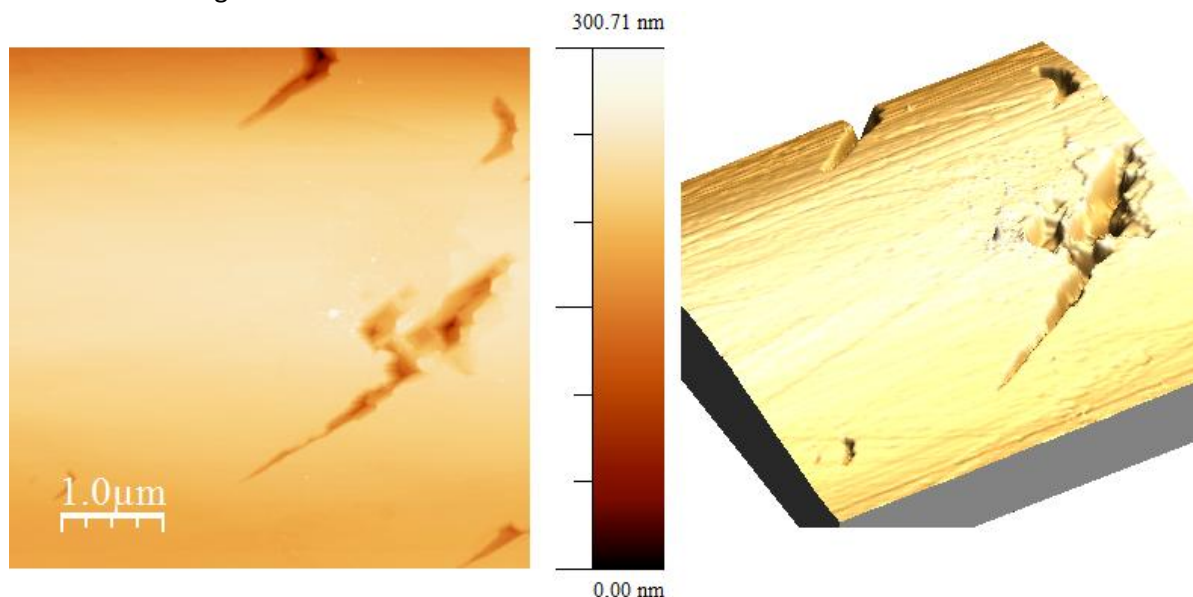


Figure 3.6: A $5 \times 5 \mu\text{m}$ AFM picture of sample **4** post-etch, in 2D and 3D. Only a small amount of etching has occurred around the surface defects.

Sample **5** (figure 3.7), despite running smoothly in the reactor, could not be imaged well on the AFM, appearing to be covered in small spikes or spots of unknown origin. This happened on multiple occasions on two different AFM set-ups. The samples were cleaned by refluxing in aqua regia for 15 minutes (using the same method as stated previously), to remove any foreign material from the surface, however this did not improve the image quality. It is possible on some images to see the occasional etch pit, but accurate measurements could not be made. This suggests that 25 minutes is approximately the right amount of time to obtain measurable etch pits at 125 Torr. However due to the imaging problems, for the purpose of this investigation the sample was discounted.

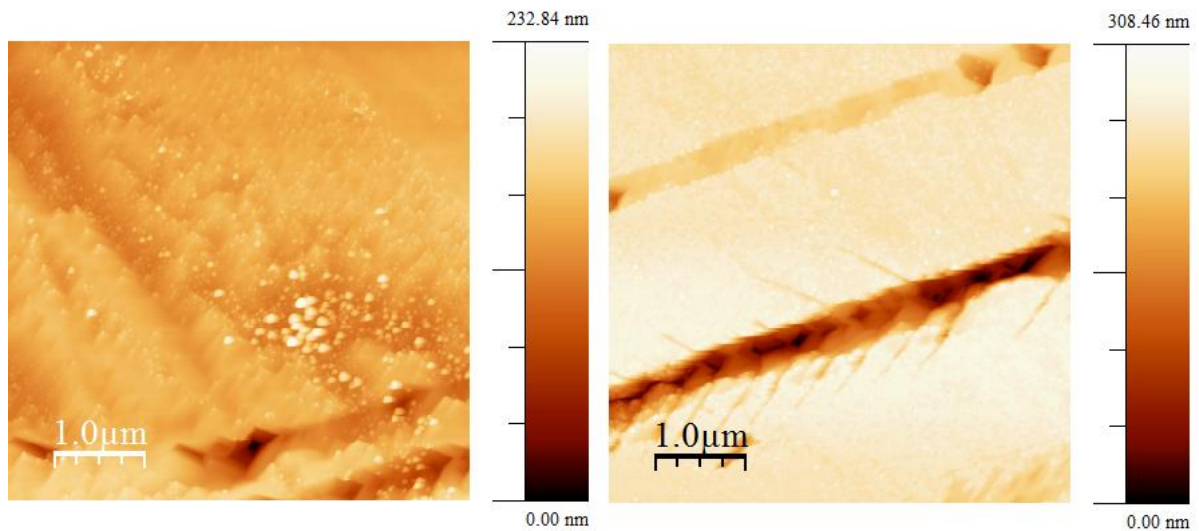


Figure 3.7: Two $5 \times 5 \mu\text{m}$ images of sample 5. All images showed the diamond surface to be covered in a range of unknown features. It is possible to see some square etch pit like shapes on both of these images.

Sample 6 (figure 3.8) was covered in larger rectangular etch pits of varying shapes and sizes. Many etch pits overlapped or formed at the base of existing pits, making measurement difficult since it was often hard to determine the centre of the etch pit. This shows the etching process shortly before the large scale smoothing seen in sample 2, as etch pits collide and the upper layers begin to etch away rapidly, confirming our current conclusions and our understanding of the why etching is anisotropic.

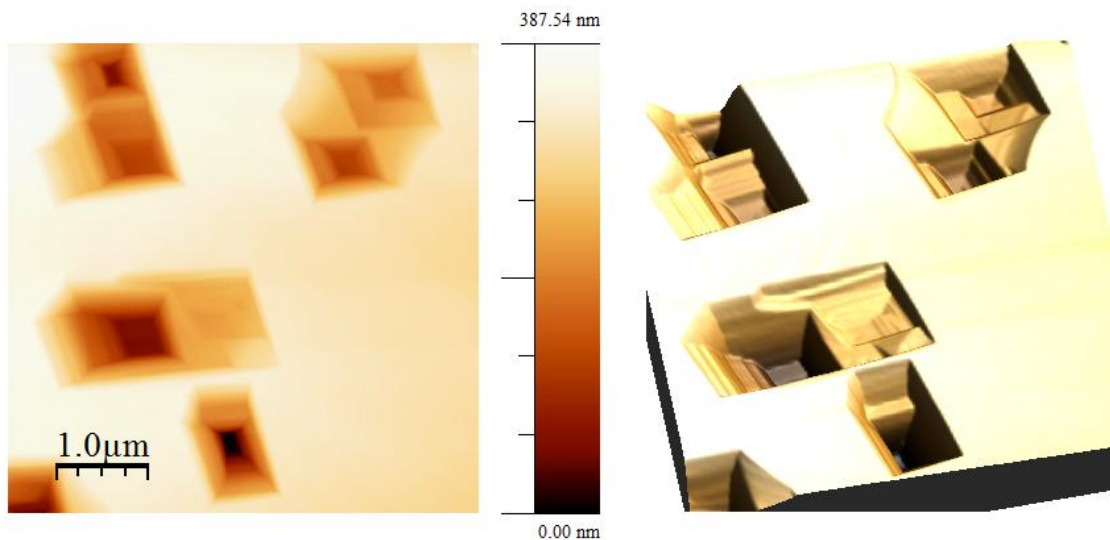


Figure 3.8: A $5 \times 5 \mu\text{m}$ AFM picture of sample 6 post-etch, in 2D and 3D. The picture shows several large etch pits, some of which overlap. In the top right it is possible to see that two etch pits have collided, and the upper layers surrounding the point of collision have begun to etch away rapidly across the surface.

Sample	Pressure / Torr	Etch pit density / μm^{-2}	Average width / nm	Average depth / nm	Lateral : Vertical etch rate ratio
1	100	0.653	374	27	7 : 1
3	150	0.570	166	41	2:1
6	150	0.189	670	141	2.4 : 1

Table 3.2: The etch pit density, dimensions and the etch rate ratios for Samples 1, 3 and 6.

It is also worth highlighting that the measured lateral etch rates do not include the etching of S_B steps, since the etch pit walls are only comprised of D_A edges. The lateral etching of S_B edges is extremely fast, as observed on samples 2 and 3, where etch pits have grown into each other, exposing the S_B ends of dimer rows, leading to the removal of entire layers in a matter of minutes.

We can see from samples 1 and 4 that the lateral and vertical etch rates are not constant throughout the period of etching. Sample 4 showed no etch pits at all, compared to the relatively large, well defined etch pits on 1, suggesting the etching began part way through the run, with etch pits forming and growing in the final 5 minutes. Interestingly the lateral and vertical etch rate ratios of samples 3 and 6 are roughly the same, which suggests that even though the individual etch rates change during the etching period, they change at the same relative rate. Thus it can be concluded that the etch rate ratio does not change with time.

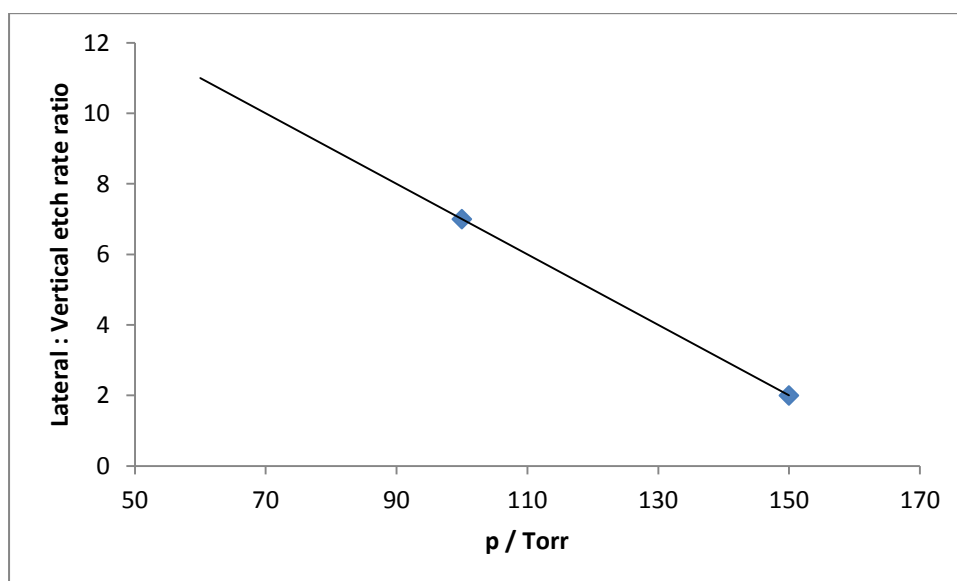


Figure 3.9: Plot of the lateral : vertical etch rate ratio as a function of pressure (p).

The only data that can be used to investigate the relationship between reactor pressure (p) and the etch rate ratio is the data from samples 1 and 3, the only samples to produce measurable etch pits over the same period of time. Figure 3.9 shows this relationship using the data collected from these two samples. As with the diamond : graphite etch rate investigation, having two data points only allows a linear relationship to be modelled, which isn't necessarily true. The approximate linear relationship is:

$$\text{Lateral : Vertical etch rate ratio} = -0.1p + 17 \quad (2)$$

In general, as pressure increases, the diamond etch rate increase as hydrogen atoms impact upon the surface more frequently. This negative relationship shows that the vertical etch rate increases more rapidly than the lateral etch rate as the pressure increases. Assuming that sample **3** is showing that new etch pits that have just begun to grow as the upper diamond layers have been completely etched away, it isn't possible to measure and compare the individual lateral and vertical etch rates to see how they vary with pressure, since the actual time taken to etch the individual pits is unknown.

This investigation provided a good first approximation of how the ratio between the lateral and vertical etch rates varies with pressure, and showed that it does not vary significantly with time. However more work needs to be carried out before these conclusions can be confirmed and the linear relationship can be assumed to be accurate. Etch pit growth is unpredictable at best, which certainly limited the effectiveness of this part of the project. Whilst the runs did back up our theories on the mechanisms of diamond etching, only three samples produced any measurable data, despite being well within the ranges in which etch pits can form, according to the literature. Repeating the etching experiments with the same conditions would be worthwhile, to see if they are consistent with the current results and thus if they can be validated, but as stated before, etch pits will only form over a narrow band of conditions. Whilst, when they do form, they provide an ideal way to compare the lateral and vertical etch rates, it is important to identify a different method to measure the etch rates over the much wider range of conditions that can be used for diamond growth, in order for a detailed model of diamond etching and growth is to be produced.

3.3 Computational Studies into the Mechanism of Etching

Discovering a plausible mechanism by which diamond is etched from the (100) surface is of clear importance to understanding diamond etching and creating a working model of diamond growth. It could also provide insight into how many of the experimentally observed phenomena arise during etching, for example the formation of etch pits, smooth S_A and rough S_B edges.

Previous computational investigations have proposed various potential mechanisms but none of these were completely satisfactory, necessitating the need for a new mechanism. The work by Frenklach *et al*^[4] seemed the most plausible and comprehensive investigation into the subject. His proposed mechanism however was flawed in places, with structures containing penta-valent carbons and multiple radicals in close proximity to each other, which are not possible or at least extremely improbable when applying a basic understanding of chemistry. The final steps, in which carbon is finally removed from the surface as either a 1 or 2 carbon species starting from a dangling bond, were chemically sound. It was decided that these final steps would be kept, but a new mechanism would be needed to rearrange a dimer into a dangling bond. The final mechanism, based on the reverse of a growth mechanism proposed by Cheesman *et al*^[5] in which a reconstructed dimer is formed, is a series of atomic hydrogen additions and abstractions to and from the surface, and structural transformations, all of which are reversible (*figure 3.10*). The various final steps proposed by Frenklach were satisfactory, so only the simplest process, in which carbon is removed

as a methyl radical was looked at initially. The other routes, etching one or two carbon species, would be investigated at a later date.

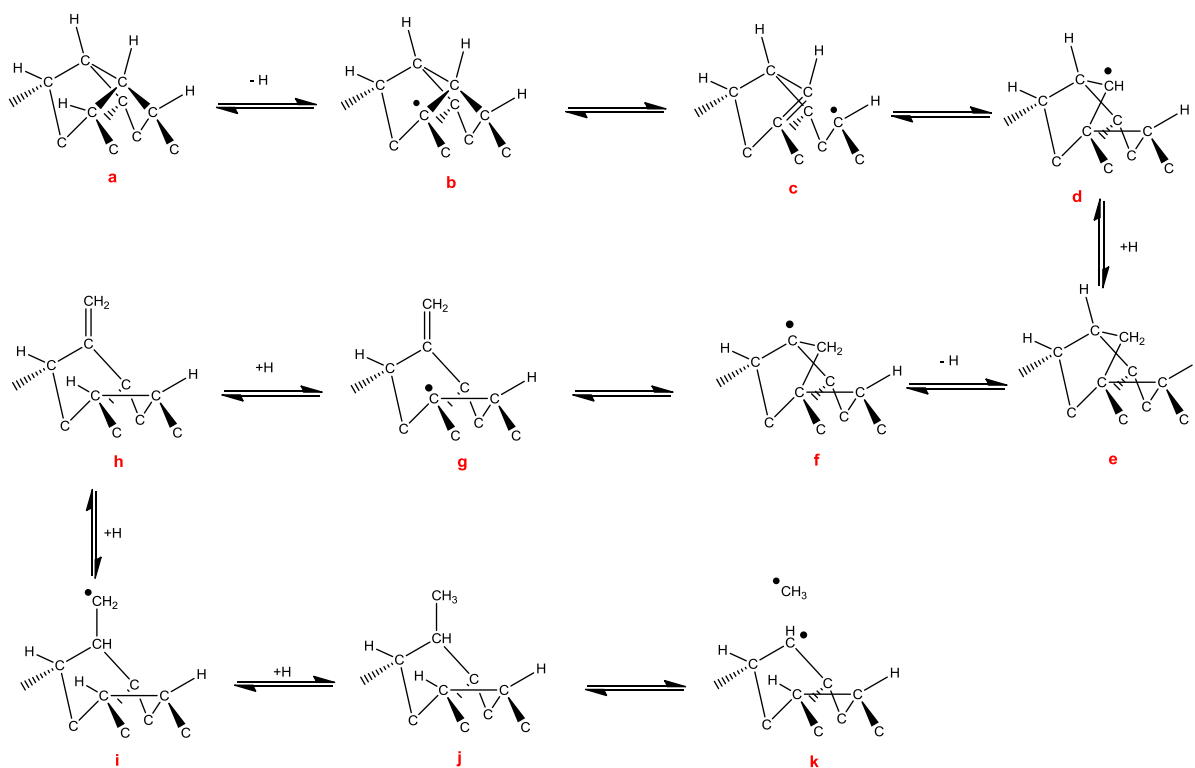


Figure 3.10: The proposed etching mechanism.

The proposed mechanism was investigated and tested using two computational techniques. A series of quick, semi-empirical PM3 calculations were used to initially test the plausibility of the mechanism, this was followed by more accurate yet more computationally expensive *ab initio* calculations based on density functional theory (DFT).

3.3.1 Semi-Empirical (PM3) Calculations

Semi-empirical PM3 level calculations were used to initially gauge the plausibility of the mechanism. PM3 (Paramater Method 3) is a method of optimizing structural parameters, and is a member of the MNDO-AM1 family of calculations. Based on Hartree-Fock theory, the use of empirically derived and optimised parameters drastically increase the speed of calculation, which would be significantly more expensive using full *ab initio* calculations. The calculated energies, vibrational frequencies and optimised structures are not as accurate as those from more theoretically pure methods, but they provide a good enough first approximation to identify any problems with the mechanism. Calculations were run for each step of the mechanism and the transition states using both the smaller and large diamond clusters (*figure 2.4*). The larger cluster models a larger region of the diamond (100) surface, and imposes more restrictions on the bending of the cluster, making it more similar to an actual (100) diamond surface.

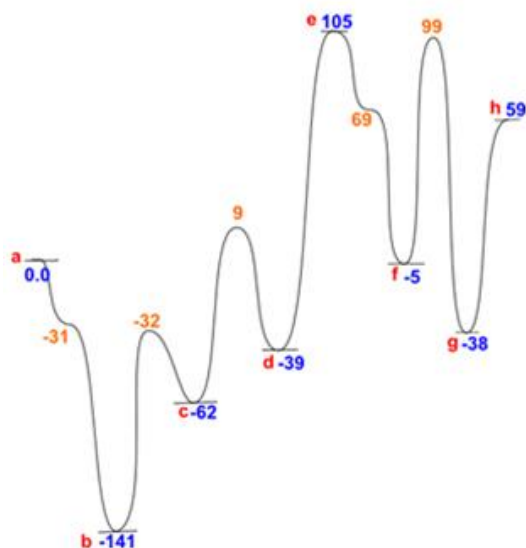


Figure 3.11 The potential energy surface (PES) illustrating the rearrangement of a reconstructed dimer on a diamond (100) surface (**a**) to a dangling carbon double bond (**h**), prior to removal of a methyl radical, modelled using PM3 level calculations and the smaller cluster (figure 2.3). The energies are in kJ mol^{-1} relative to **a** (137 kJ mol^{-1}). Optimised structure energies are in blue and transition states are in orange.

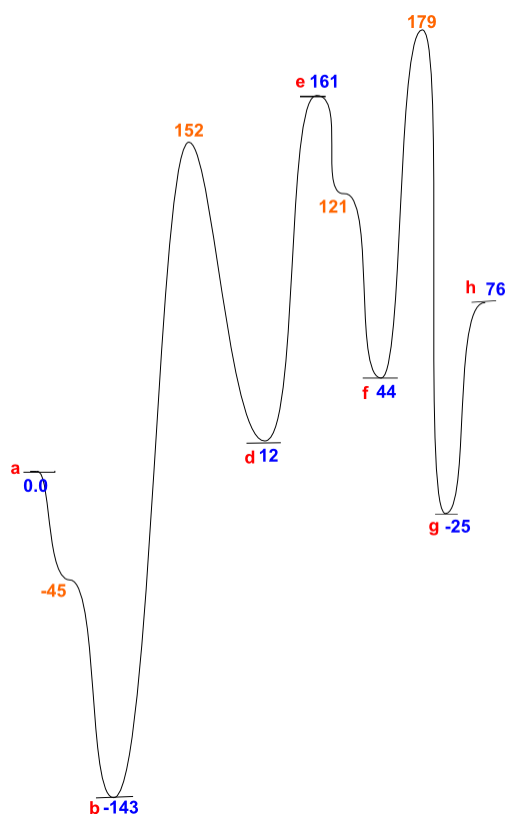


Figure 3.12: The potential energy surface (PES) illustrating the rearrangement of a reconstructed dimer on a diamond (100) surface (**a**) to a dangling carbon double bond (**h**), prior to removal of a methyl radical, modelled using PM3 level calculations and the bigger cluster (figure 2.4). The energies are in kJ mol^{-1} relative to **a** (1450 kJ mol^{-1}). Optimised structure energies are in blue and transition states are in orange.

Steps involving the addition of atomic hydrogen or a methyl radical to a radical site are barrierless^[5], hence the lack of a transition state energy for steps **d-e** and **g-h**. Transition states identities were confirmed by analysing the vibrational modes of the optimised structures, and observing a large, negative vibrational frequency. The negative frequency indicates that the reaction coordinate in question corresponds to a maximum on the potential energy surface (PES), and thus a transition state.

Interestingly energies for structure **c** could not be found when using the bigger cluster, instead being optimised to either structures **b** or **d**, even though the smaller cluster had no problem optimising **c**. There are two plausible reasons for this: Firstly, **c** sits between **b** and **d** energetically, with relatively small barriers on either side. When the structure is optimised for the large cluster, it instead treats **c** as part of the PES between **b** and **d**, and so optimises the structure to **b**, which is lower in energy. Secondly, the smaller cluster is significantly more flexible than the large cluster, so is able to distort the structure of **c** during optimisation, lowering it in energy so it can be successfully modelled. Because of these reasons, the fact that structure **c** cannot be optimised by the larger cluster does not necessarily mean it does not exist, and the problem instead lies with the limitations of the method of calculation.

Overall the mechanism appears plausible based on this data, when the inaccuracies of PM3 calculations are considered, and the fact that thermodynamic and entropic energy effects are not taken into account, all of the energies required are not unrealistic. All steps are low enough to be attainable under CVD conditions, albeit slowly, as is to be expected when etching diamond which is itself a very slow process. The only exception might be the **b-d** barrier on the large cluster, but with **c** in between this would in reality be two separate, smaller steps.

3.3.2 Density Functional Theory (DFT) Calculations

The next set of calculations used much more rigorous *ab initio* methods based on Density Functional Theory (DFT) to obtain significantly more accurate energies and vibrational frequencies for optimised structures and transition states. Since the calculations are theoretically pure, not using any experimentally derived parameters, they are much more expensive and as such using the larger cluster became unrealistic for the time constraints of this short project as calculations required more than 200 hours to complete. As such only the smaller cluster was used at this stage (*figure 2.3*).

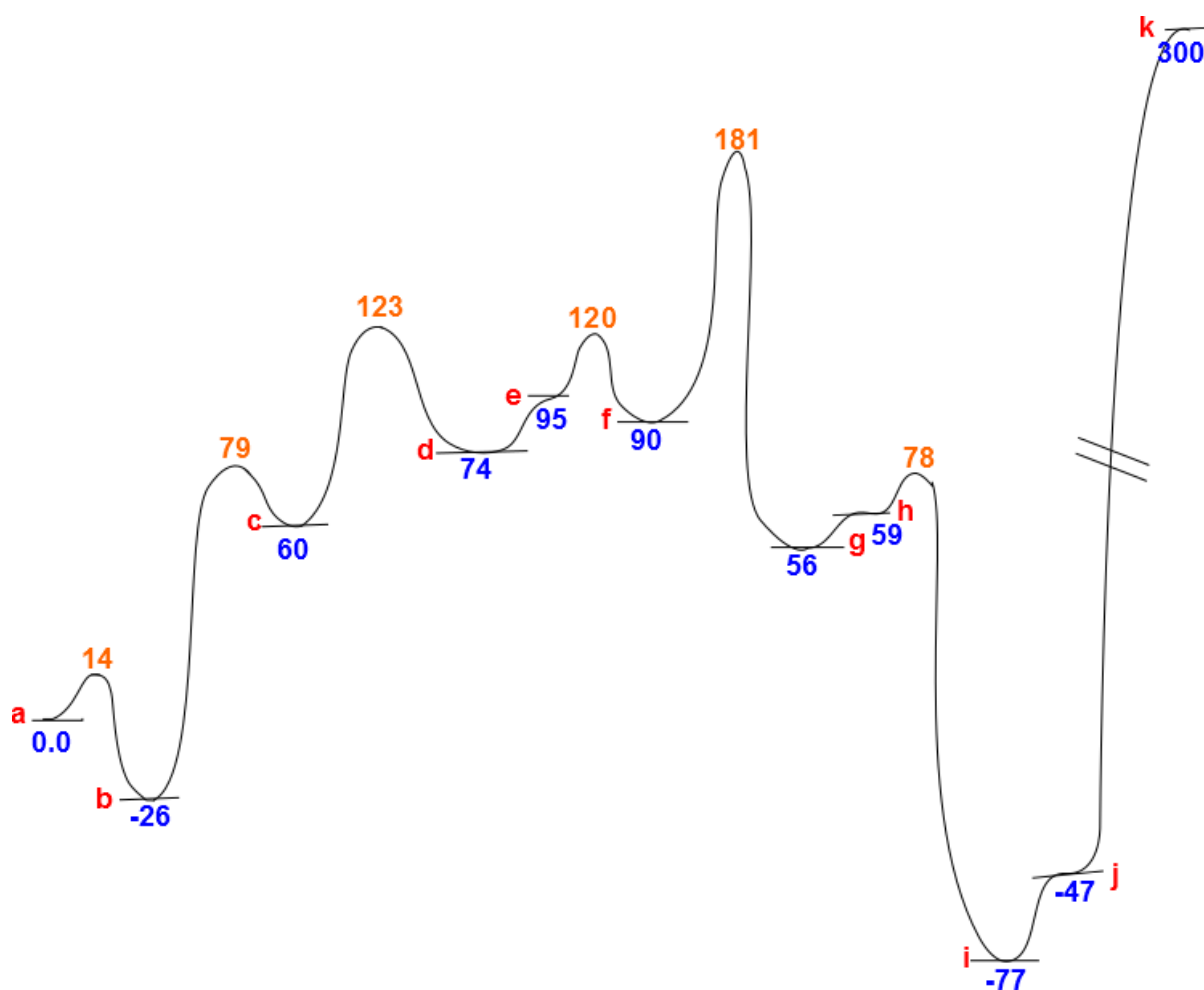


Figure 3.13: The potential energy surface (PES) illustrating the rearrangement of a reconstructed dimer on a diamond (100) surface (**a**) to a dangling carbon double bond (**h**), followed by the removal of a methyl radical (**k**), modelled using DFT. The energies are in kJ mol^{-1} relative to **a**. Optimised structure energies are in blue and transition states are in orange. Starting energy of **a** = $-1.74 \times 10^6 \text{ kJ mol}^{-1}$

The energies required for each individual step are relatively small, with the maximum energy needed for a single step of 105 kJ mol^{-1} , discounting the final step to be discussed later. Energies of these magnitudes would be easily attainable under CVD conditions, so the dimer rearrangement mechanism is certainly energetically feasible. The last step (**j** – **k**), is the dissociation of a C-C covalent bond and requires by far the largest amount of energy. At over 300 kJ mol^{-1} , this seems to indicate that the actual etching of a one carbon species from the diamond surface is unrealistic. However, the DFT calculations made do not take into account the thermodynamics and entropy changes involved and so the large increase in entropy alone on removing a methyl radical from the diamond surface, makes this final step much more realistic.

Overall this is a realistic mechanism for the etching of carbon from the 2×1 reconstructed diamond (100) surface. Each individual structure has been successfully modelled and optimised, each step being energetically reasonable and transition states existing where expected. DFT has been a useful tool when investigating the mechanism of etching the diamond (100) surface, although it is not a

fully comprehensive model, requiring thermodynamic and entropic energy effects to be considered as well.

Closer inspection of the mechanism also sheds light on some of the features of the (100) surface and why anisotropic etching is observed. The first crucial step (**a-b**) is the abstraction of hydrogen from one of the carbons bound to the surface dimer, in the layer below the surface. Most dimers will not have a hydrogen atom bound to their neighbouring carbons; these will instead be bound to the next dimer in the row. As a result it is impossible to etch these dimers using this mechanism, until one of its neighbouring dimers is removed. This explains several things: why large straight S_A steps are observed, where it is impossible to etch into the side of a dimer row; why rough S_B steps are observed, where the dimers on the edge have two hydrogen atoms available to initiate the etching making it relatively facile; and why smooth plateaus can be seen, where vertical etching is impossible. A rough approximation of the relative etch rate of dimers would be that a lone dimer on the surface, such as the one used in the computational calculations, etches twice as fast as one at the end of a dimer row since it has twice as many hydrogen atoms available for initiation.

It is worth noting that whilst the mechanism is certainly plausible, it is not the only mechanism by which diamond is etched. The proposed mechanism alone will probably not account for all the experimentally observed etch rates. As mentioned earlier in the report, various groups used computational methods to model other diamond growth mechanisms, such as the initial insertion of a methyl radical into a dimer C-C bond, via a ring opening/closing mechanism^[5-8], and the insertion of a methyl into the a trough between two successive dimers in a chain^[5,9]. The reverse of both of these could be used as the basis for additional etching mechanism investigations.

The next logical step for this investigation would be to use Quantum Mechanics / Molecular Mechanics (QM/MM) methods to model the mechanism at different surface features. QM/MM allows the modelling of a large region of a diamond surface using simple molecular mechanics, which is computationally cheap, and a small cluster within the region using quantum mechanics. This allows us to observe the effect being in a large surface feature has on the small region, without the calculations being too expensive.

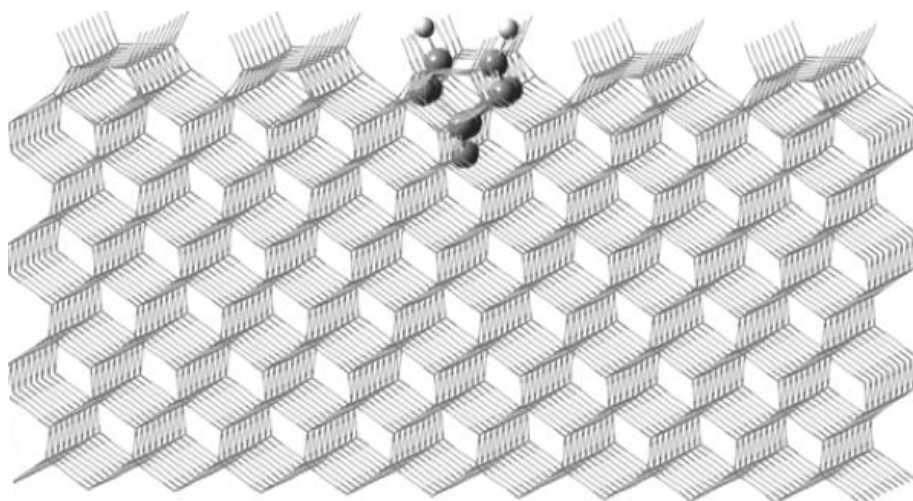


Figure 3.14 An example of a diamond QM/MM model, showing the large MM region (diamond lattice) and the small central QM region (ball and stick C_9H_{14} cluster) used to model a dimer on the diamond (100) surface^[10].

By modelling the small cluster within various large surface features at various stages of the etching mechanism, it would be possible to see how the location of the cluster effects the energies required for each step, and in turn how likely the dimer will etch. Dimers could be modelled on a S_A or S_B step of varying sizes, within a perfectly smooth surface or on a corner of a plateau (the edge of both an S_A and S_B step) amongst many others. This could help explain many of the phenomenon observed during etching, or confirm the conclusions previously drawn, and provide relative rates of etching at each location.

3.4 References

- [1] Donnelly C.M., *et al. Diamond and Relative Materials*, 6 (1997), 787-790
- [2] Jiang X., Rickers C., *Appl. Phys. Lett.* 75 (1999) 3935.
- [3] Mitsuhashi M., Karasawa S., Ohya S., Togashi F., *Appl. Surf. Sci.* 60/61 (1992) 565.
- [4] Netto A., Frenklach, M., *Diam. Rel. Mater.*, 14, 10 (2005), 1630
- [5] Cheesman, A., Harvey, J.N., Ashfold, M.N.R., *J. Phys. Chem. A.*, 112 (2008), 11436
- [6] Battaile C.C. *et al*, *J. Chem. Phys*, 111 (1999), 4291
- [7] Garrison B.J., Dawnkaski E.J., Srivastava D., Brenner D.W., *Science* 255 (1992), 835
- [8] Oleinik, I.I., Pettifor, D.G., Sutton, A.P., Butler, J.E., *Diam. Rel. Mater.*, 9 (2000), 241
- [9] Harris, S.J., *Appl. Phys. Lett.*, 56 (1990), 2298
- [10] Halliwell, S., MSci Thesis, University of Bristol, 2012 "Investigations into the plasma formed by a microwave reactor used for the chemical vapour deposition of diamond" available from <http://www.chm.bris.ac.uk/pt/diamond/>

Chapter 4 – Afterword

4.1. Conclusion

In order to accurately model and predict how diamond will grow during CVD growth it is essential to fully understand each individual part of the process. The work presented in this thesis has taken an in depth look at the etching of diamond by atomic hydrogen that occurs during CVD diamond growth. The relative etch rates of graphite and diamond were investigated with initial results suggesting that graphite etches roughly 200 times faster than diamond at reactor pressures of 100 Torr, although further investigation was prevented by problems during etching.

The etching of the 2 x 1 (100) reconstructed diamond surface was investigated in order to find the relative rates of etching parallel and perpendicular to the diamond surface. AFM analysis showed square etch pits had formed on the diamond surface. A lateral to vertical etch rate ratio of 7:1 was calculated with a reactor pressure of 100 Torr, and this ratio reduced as pressure increased. This result confirms that that diamond etches faster laterally than vertically, which reflects that once a dimer is removed from the surface, it is much easier to etch laterally than it is to remove a dimer from the layer below. It was also shown that during etching the diamond surface goes through a cycle of phases; firstly etch pits form on the diamond surface, which then grow and overlap, leading to rapid lateral etching along the dimer rows and ultimately the total removal of several diamond layers to form a smooth surface. The cycle then repeats as etch pits form on the new surface.

A combination of semi-empirical PM3 calculations and DFT calculations were used to successfully model a mechanism by which carbon is removed from a reconstructed dimer on the (100) diamond surface, in the form of methyl radical. Energy minima and transition states were calculated for a series of atomic hydrogen additions, abstractions and structural rearrangements. The energies for each individual step was found to be of a low enough value that the reaction is plausible under CVD conditions, albeit at a slow rate, as is to be expected for the etching of diamond

4.2. Future Work

An ongoing project within the University of Bristol Diamond Group aims to create a full kinetic Monte Carlo simulation of CVD diamond growth over the full range CVD growth conditions. This model would allow accurate predictions of rates of diamond growth and the properties of final diamond substrate, and explain how and why diamond grows as it does under certain conditions. The data produced in this thesis has provided preliminary experimental values for rates of etching which will be of use to this project.

As already mentioned there are many opportunities for further work. The graphite–diamond etch rate investigation was brought to a halt before it could be completed; the etch ratio of 200:1 is a good first impression but is only truly accurate for etching at 100 Torr. Upon the arrival of the new

sample stage this section can continue, and be expanded over the wider range of conditions CVD diamond growth can operate under to see how the graphite-diamond etch ratio varies as pressure, microwave power and etching time change. Running repeats will increase the reliability of the results.

The investigation into the etch rate parallel and perpendicular to the (100) diamond surface would also benefit from expanding the range of etching conditions. Etch pits will only form over a relatively small section of the potential range of CVD conditions, so a new methodology is required to identify a starting point for etching and more accurately measure the individual etch rates. The lateral etch rate measured from etch pit dimensions also does not take into account the etching of S_B edges, which is also necessary for the final growth simulation.

Further computational investigations would be useful in obtaining approximate relative etch rates. Using QM/MM methods to model the etching mechanism at various surface features, such as S_A and S_B step edges, lone dimers and dimers embedded in a smooth surface, will give reasonably accurate relative energies for etching each feature. From this the relative rates of etching, via this mechanism, at each surface feature, can be calculated. This is not the only mechanism by which atomic hydrogen etches diamond; there have been several growth mechanisms proposed and applying a similar approach to the one used in this section of the report, more etching mechanisms could be produced. Combined together these would provide a comprehensive look at the relative etch rates of different surface features, and vastly improve the computational simulation of diamond growth.

Looking away from reactions on the surface, it would be interesting to investigate the gaseous species removed from the surface during etching. Spectroscopic techniques could be effectively used to analyse the composition of the plasma. Further analytical techniques to be used could include mass spectroscopy, cavity ring-down spectroscopy or optical emission spectroscopy as has been effectively used in other research into diamond growth using a microwave reactor ^[1,2]. The fate of species originating from the diamond surface is also of interest, as many will fall back to the surface and could play a part in various processes, such as smoothing.

4.3. Acknowledgements

I would like to thank Element Six Ltd. for the generous long-term loan of the microwave CVD reactor used throughout this project.

I would like to give a special thanks to Professor Paul May, my supervisor, for his advice and encouragement throughout this project. Thanks also go to my secondary assessor, Dr Neil Fox for his support. To Sarah Halliwell, for her invaluable guidance and assistance in the laboratory and during the writing of this thesis. To Professor Jeremy Harvey and Jeff Rodgers for their help with the computational investigation, and teaching me the necessary techniques, and to Rob Harniman for sharing his knowledge of atomic force microscopy.

Finally a big thank you to all the other BUDGies in the Bristol University diamond group, for making this project such an enjoyable experience!

4.4. References

[1] Halliwell, S., MSci Thesis, University of Bristol, 2012 “Investigations into the plasma formed by a microwave reactor used for the chemical vapour deposition of diamond” available from <http://www.chm.bris.ac.uk/pt/diamond/>

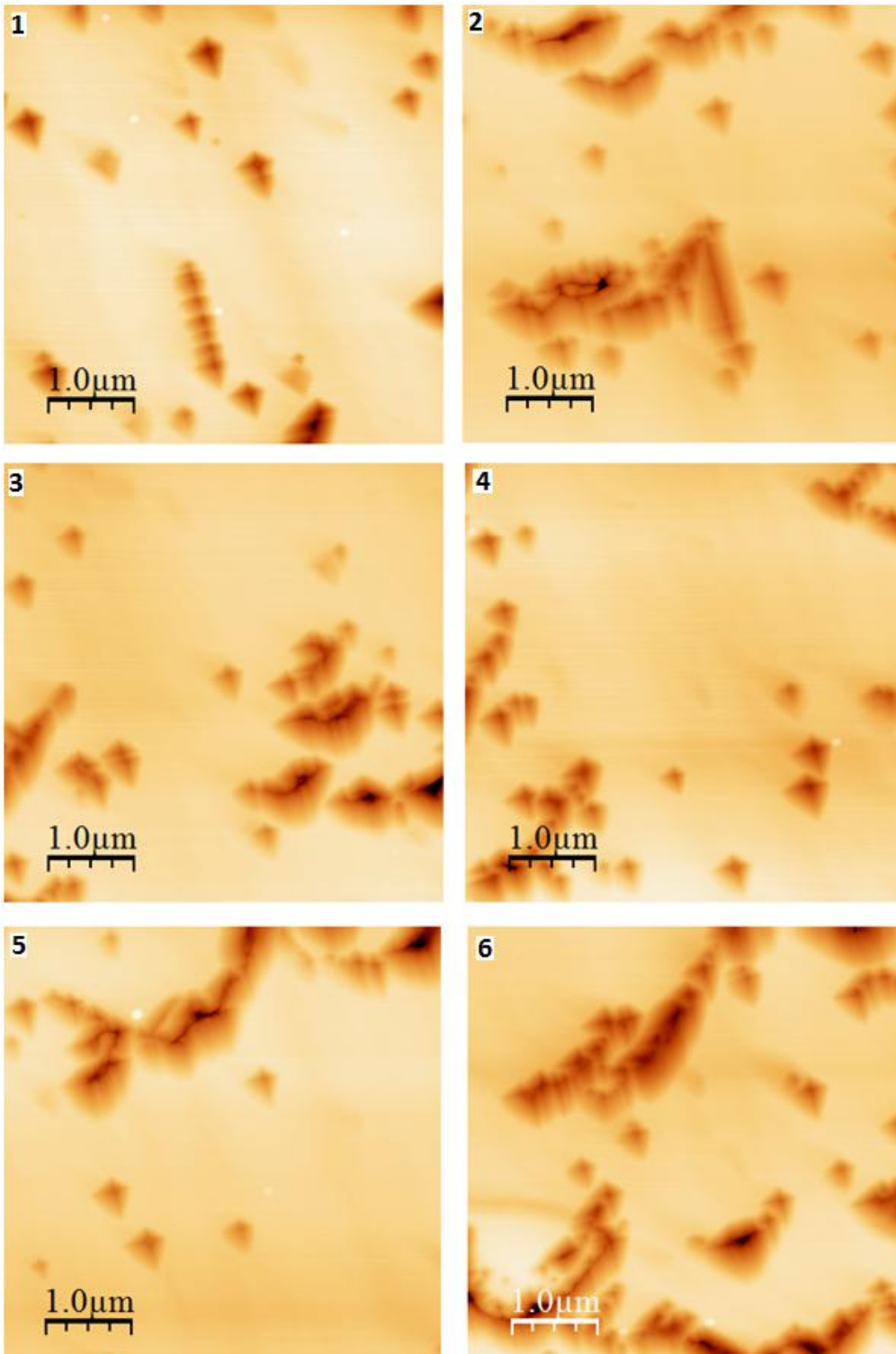
[2] Ma, J., Richley, J.C., Ashfold, M.N.R., Mankelevich, Yu.A., *J. Appl. Phys.* 104 (2008) 103305

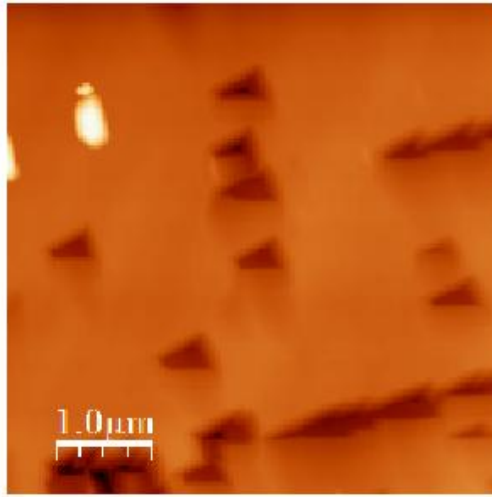
Appendices

Appendix A

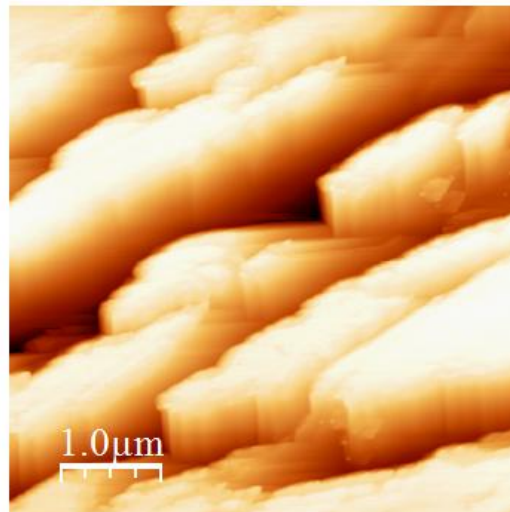
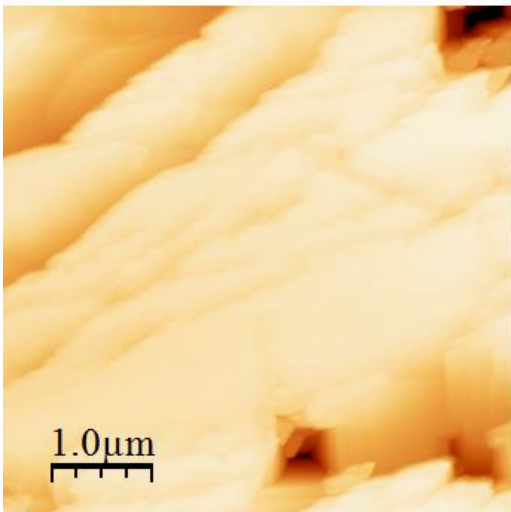
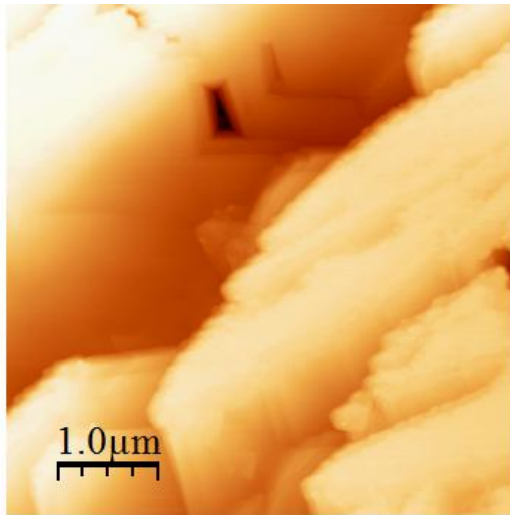
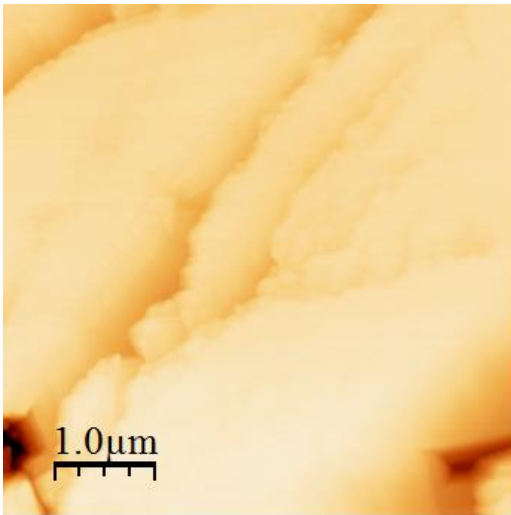
All AFM images for SCD samples 1-6. Images that were considered for etch pit analysis have been numbered in accordance with the data in *Appendix B*.

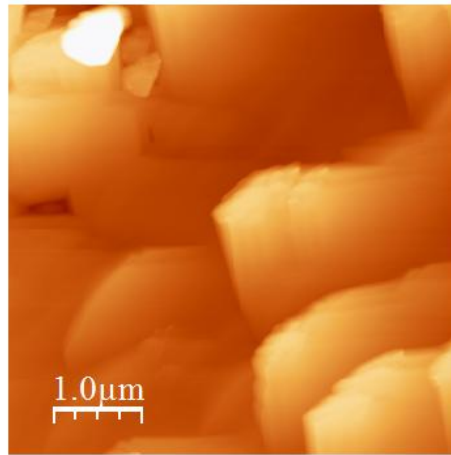
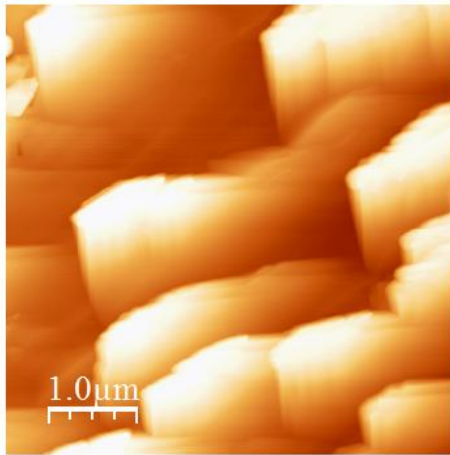
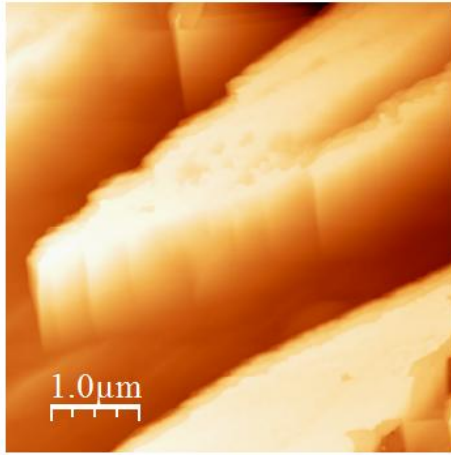
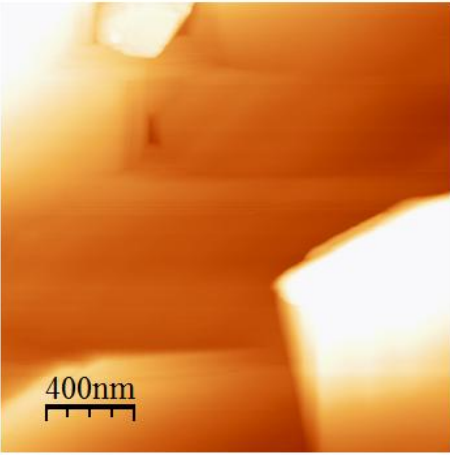
Sample 1



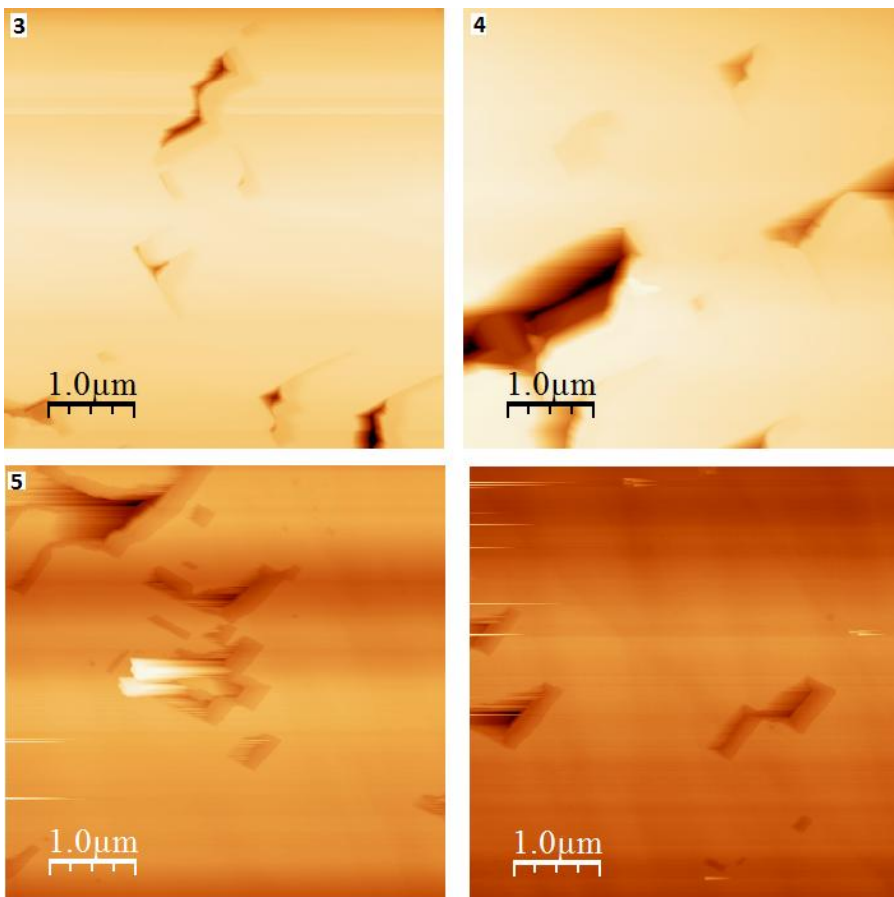
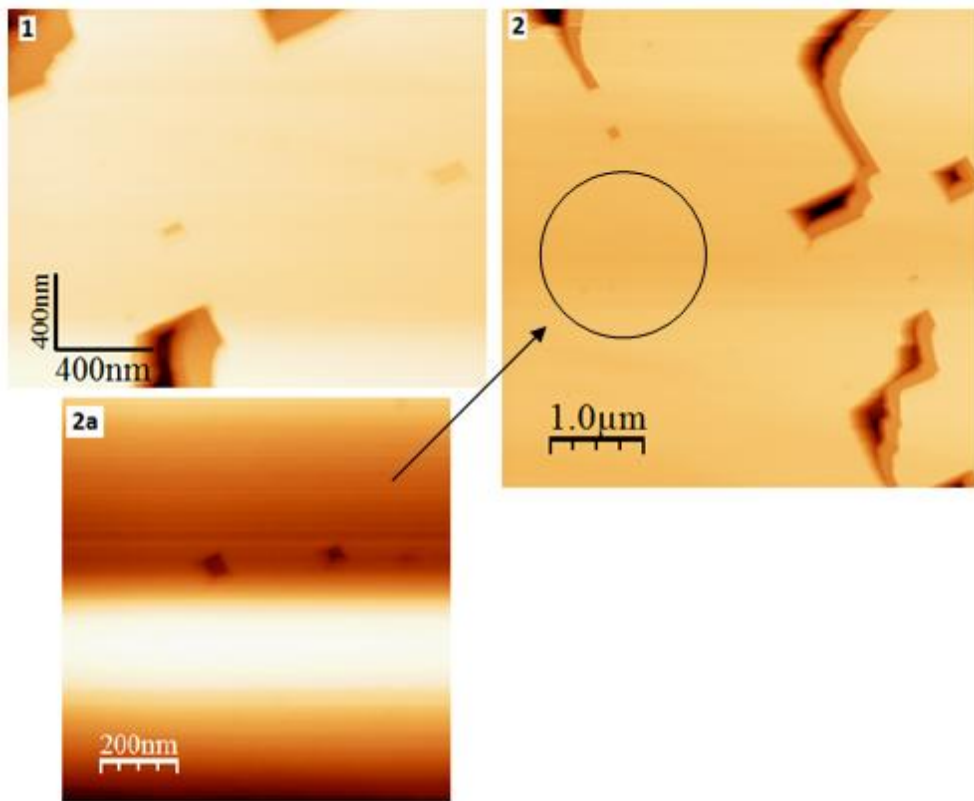


Sample 2

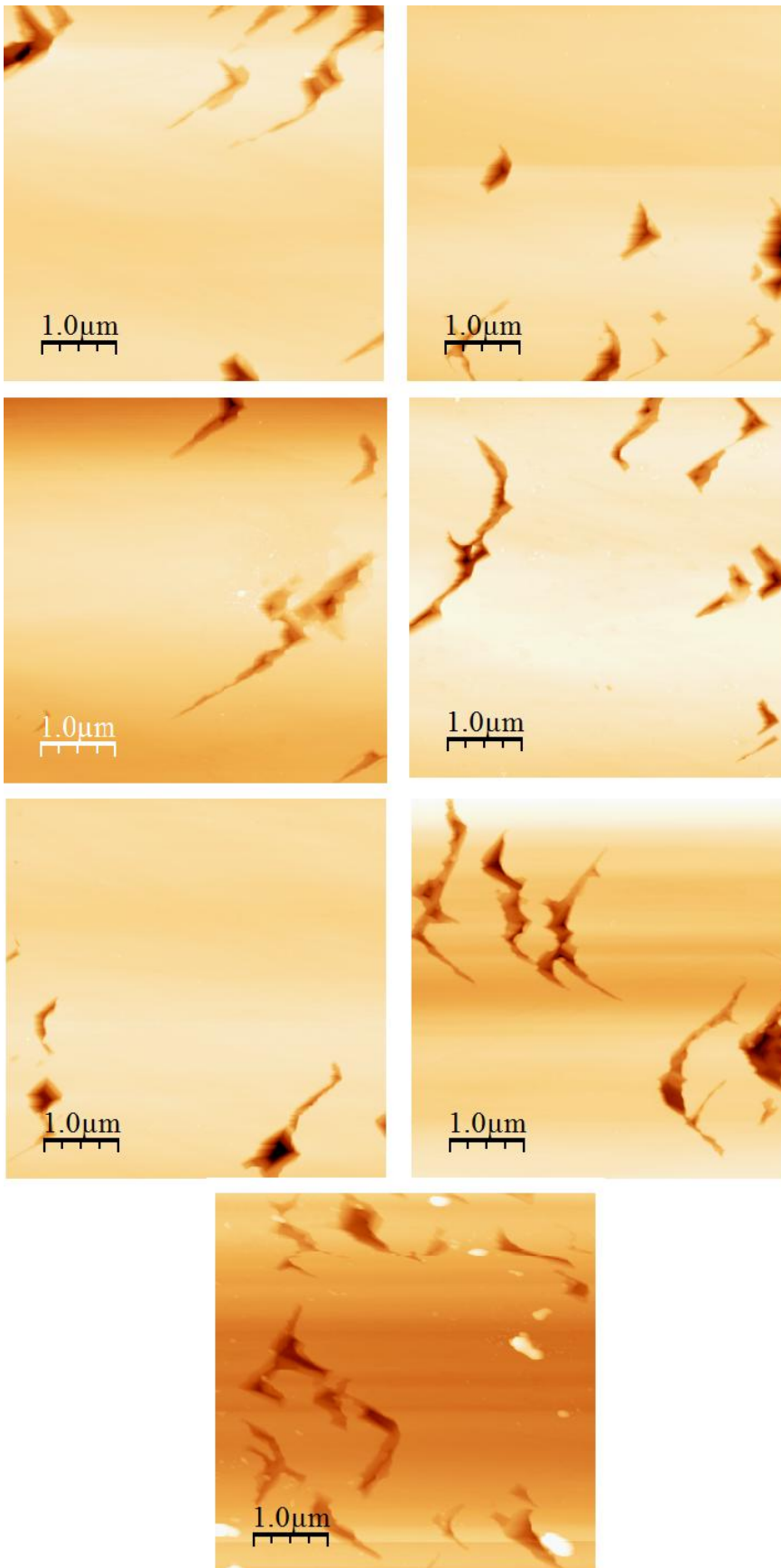




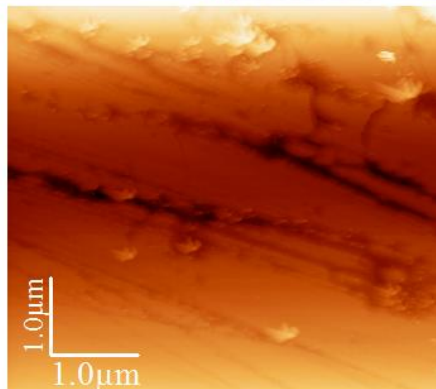
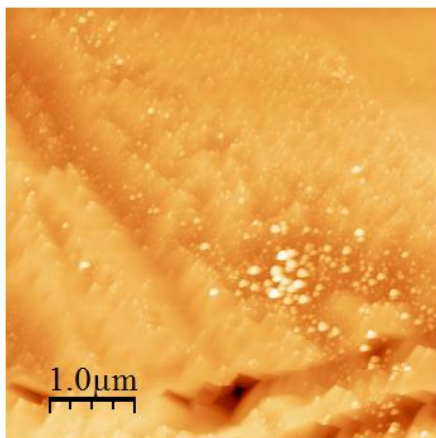
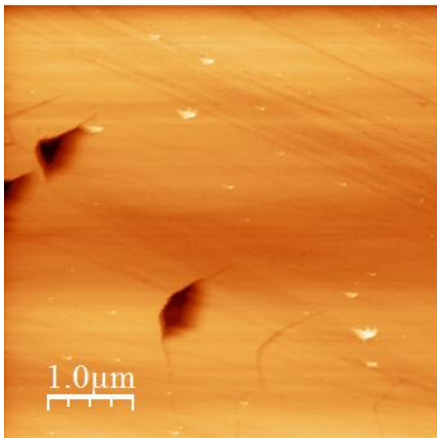
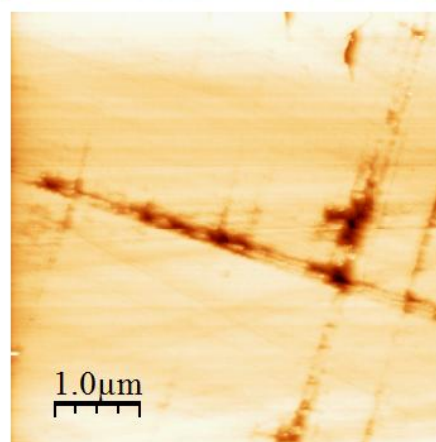
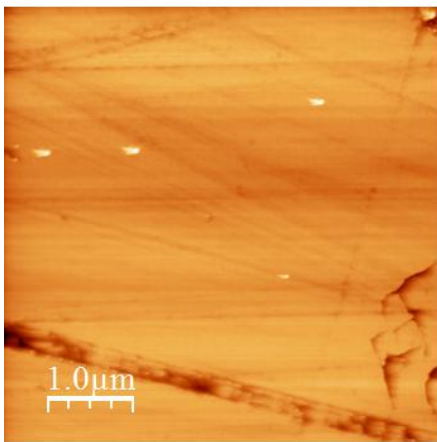
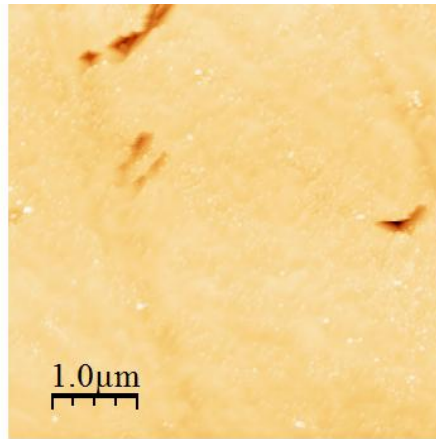
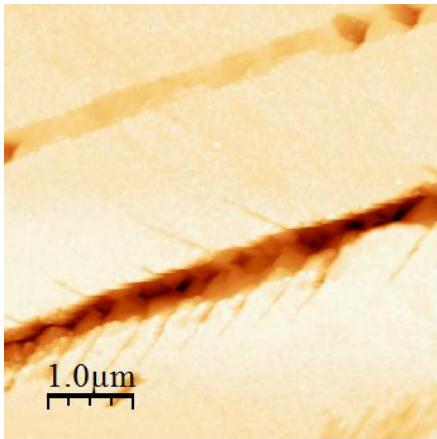
Sample 3



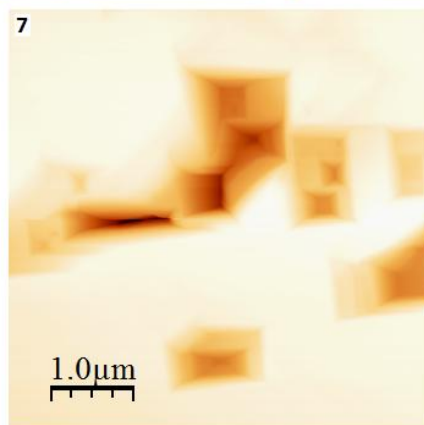
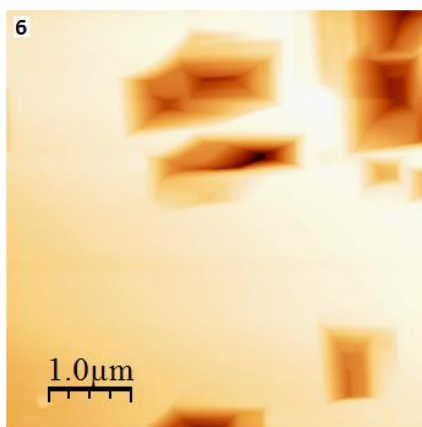
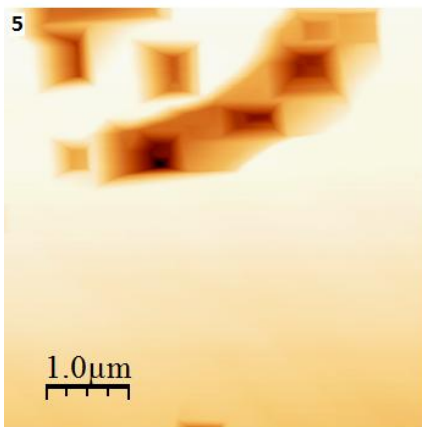
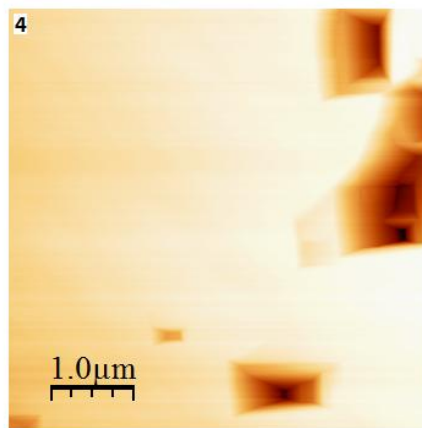
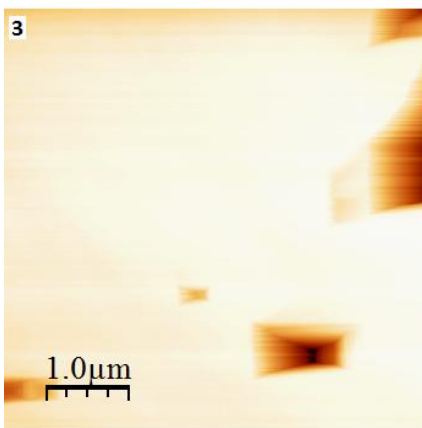
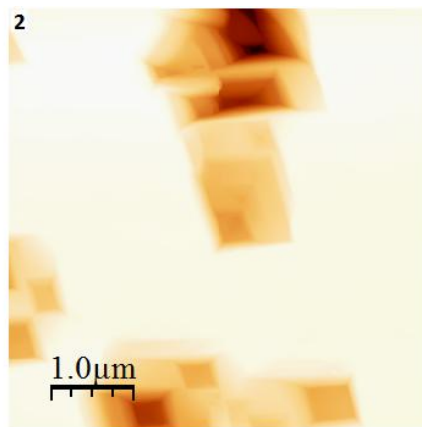
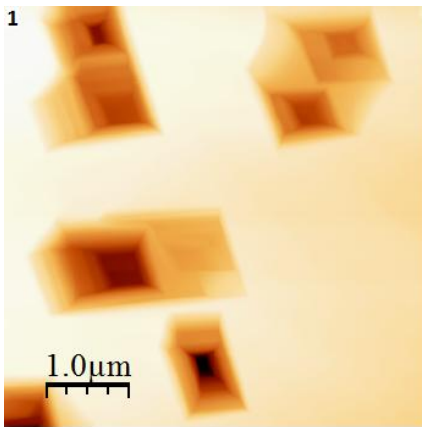
Sample 4

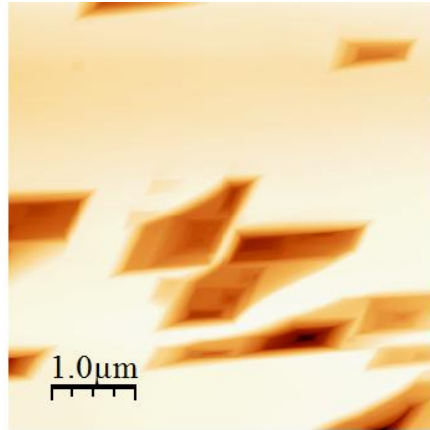
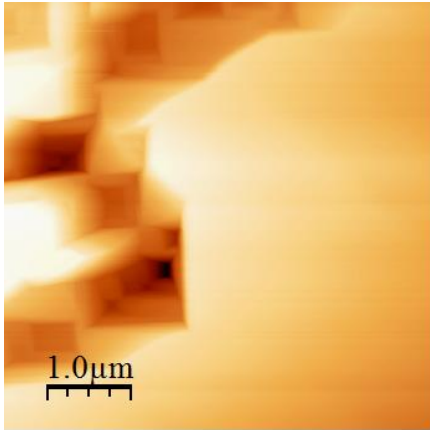


Sample 5



Sample 6





Appendix B

Tables showing the etch pit data from each individual AFM image obtained from samples **1,3** and **6**.

Sample 1

Picture 1:

Number of etch pits	Average width /nm	Average depth /nm	Length : Depth Ratio
25	380.0	28.4	6.69

Etch Pit	Length /nm	Depth /nm
1	450	32
2	350	25
3	450	35
4	450	35
5	450	35
6	300	15
7	400	30
8	300	25
9	250	20
10	400	32

Picture 2:

Number of etch pits	Average width /nm	Average depth /nm	Length : Depth Ratio
17	376.5	27.2	13.82

Etch pit	Length /nm	Depth /nm
1	250	23
2	325	27
3	500	35
4	400	31
5	350	20
6	350	25
7	500	43
8	350	24
9	350	21
10	325	23
11	350	25
12	375	26
13	500	35
14	400	34
15	400	31
16	350	23
17	325	17

Picture 3:

Number of etch pits	Average width /nm	Average depth /nm	Length : Depth Ratio
13	384.6	26.8	14.33

Etch pit	Length /nm	Depth /nm
1	350	23
2	400	32
3	350	23
4	400	29
5	350	28
6	500	33
7	350	26
8	425	33
9	500	35
10	300	18
11	375	24
12	325	23
13	375	22

Picture 4:

Number of etch pits	Average width /nm	Average depth /nm	Length : Depth Ratio
17	369.1	27.2	13.55

Etch pit	Length /nm	Depth /nm
1	350	17
2	300	23
3	375	26
4	400	27
5	400	33
6	300	28
7	375	30
8	325	25
9	400	25
10	400	28
11	400	27
12	350	28
13	350	23
14	450	39
15	375	33
16	300	20
17	425	31

Picture 5:

Number of etch pits	Average width /nm	Average depth /nm	Length : Depth Ratio
8	346.9	23.3	14.92

Etch pit	Length /nm	Depth /nm
1	300	17
2	225	13
3	400	31
4	300	15
5	400	31
6	400	30
7	350	23
8	400	26

Picture 6:

Number of etch pits	Average width /nm	Average depth /nm	Length : Depth Ratio
18	386.1	27.6	14.01

Etch pit	Length /nm	Depth /nm
1	375	32
2	450	32
3	400	32
4	575	37
5	325	23
6	300	21
7	400	32
8	400	30
9	350	22
10	375	25
11	375	31
12	400	26
13	400	28
14	375	25
15	400	31
16	350	23
17	300	20
18	400	26

Sample 3

Some of these images were not the standard 5x5 μm size, so the picture size has been included.

Picture 1:

Number of etch pits	Image Size / μm	Average width /nm	Average depth/nm	Length : Depth Ratio
2	2x2	140.0	13.0	10.77

Etch pit	Length /nm	Depth /nm
1	180	10
2	100	16

Picture 2:

Number of etch pits	Image Size / μm	Average width /nm	Average depth /nm	Length : Depth Ratio
4	5x5	88.8	12.4	7.17

Etch pit	Length /nm	Depth /nm
1	150	26
2	75	8
3	60	8
4	70	7.5

Picture 3:

Number of etch pits	Image Size / μm	Average width /nm	Average depth /nm	Length : Depth Ratio
1	5x5	225.0	110.0	2.05

Etch pit	Length /nm	Depth /nm
1	225	110

Picture 4:

Number of etch pits	Image Size / μm	Average width /nm	Average depth /nm	Length : Depth Ratio
1	5x5	200.0	55.0	3.64

Etch pit	Length /nm	Depth /nm
1	200	55

Picture 5:

Number of etch pits	Image Size / μm	Average width /nm	Average depth /nm	Length : Depth Ratio
1	5x5	175.0	16.0	10.94

Etch pit	Length /nm	Depth /nm
1	175	16

Sample 6

Picture 1:

Number of etch pits	Average width /nm	Average depth /nm	Length : Depth Ratio
5	880.0	230.0	3.83

Etch pit	Length /nm	Depth /nm
1	850	220
2	1350	300
3	950	300
4	750	200
5	500	130

Picture 2:

Number of etch pits	Average width /nm	Average depth /nm	Length : Depth Ratio
7	646.4	158.6	4.08

Etch pit	Length /nm	Depth /nm
1	750	180
2	475	100
3	800	250
4	600	170
5	700	150
6	450	110
7	750	150

Picture 3:

Number of etch pits	Average width /nm	Average depth /nm	Length : Depth Ratio
3	550.0	93.3	5.89

Etch pit	Length /nm	Depth /nm
1	450	70
2	300	50
3	900	160

Picture 4:

Number of etch pits	Average width /nm	Average depth /nm	Length : Depth Ratio
3	691.7	133.3	5.19

Etch pit	Length /nm	Depth /nm
1	1000	175
2	325	50
3	750	175

Picture 5:

Number of etch pits	Average width /nm	Average depth /nm	Length : Depth Ratio
7	621.4	121.4	5.12

Etch pit	Length /nm	Depth /nm
1	650	120
2	600	40
3	450	100
4	400	75
5	700	150
6	750	165
7	800	200

Picture 6:

Number of etch pits	Average width /nm	Average depth /nm	Length : Depth Ratio
4	818.8	160.0	5.12

Etch pit	Length /nm	Depth /nm
1	1100	250
2	600	110
3	800	160
4	775	120

Picture 7:

Number of etch pits	Average width /nm	Average depth /nm	Length : Depth Ratio
4	481.3	90.0	5.35

Etch pit	Length /nm	Depth /nm
1	550	110
2	325	75
3	450	90
4	600	85

Appendix C

Tables showing the original energy and energy relative to **a** of each step and transition states for the proposed etching mechanism (steps **a-h**), using semi-empirical PM3 level calculations and the smaller diamond cluster. This includes the energies calculated for atomic hydrogen additions to radical sites, which are in fact barrierless.

Structure	Energy	Relative Energy		Transition State Energy	Transition State Energy	
	Hartree	Hartree	kJ mol ⁻¹	Hartree	Hartree	kJ mol ⁻¹
a	0.0521	0.0000	0.0			
				0.0402	-0.0119	-31.2
b	-0.0016	-0.0536	-140.8			
				0.0395	-0.0126	-33.0
c	0.0282	-0.0239	-62.6			
				0.0556	0.0035	9.3
d	0.0371	-0.0150	-39.4			
				0.0763	0.0242	63.6
e	0.0922	0.0401	105.2			
				0.0783	0.0262	68.9
f	0.0503	-0.0018	-4.8			
				0.0898	0.0377	99.0
g	0.0378	-0.0143	-37.5			
				0.0637	0.0116	30.5
h	0.0775	0.0254	66.7			

Appendix D

Tables showing the original energy and energy relative to **a** of each step and transition states for the proposed etching mechanism (steps **a-h**), using semi-empirical PM3 level calculations and the larger diamond cluster. This includes the energies calculated for atomic hydrogen additions to radical sites, which are in fact barrierless.

Structure	Energy		Relative Energy		Transition State Energy	
	Hartree		Hartree	kJ mol^{-1}	Hartree	kJ mol^{-1}
a	0.5517		0.0	0.0		
					0.5358	0.0
b	0.4971		-0.1	-143.2		
					0.6098	0.1
d	0.5561		0.0	11.7		
					0.5974	0.0
e	0.6131		0.1	161.4		
					0.5977	0.0
f	0.5683		0.0	43.8		
					0.6198	0.1
g	0.5421		0.0	-25.1		
					0.5620	0.0
h	0.5806		0.0	76.0		

Appendix E

Tables showing the energies of gaseous reactants calculated using semi-empirical PM3 level calculations.

Species	Energy	
	Hartree	kJ mol^{-1}
H	0.0830	217.9165
H ₂	-0.0213	-55.92315

Appendix F

Tables showing the original energy and energy relative to **a** of each step and transition states for the proposed etching mechanism (steps **a-k**), using density functional theory with the B3LYP/6-31G (d) basis set, and the smaller diamond cluster. This includes the energies calculated for atomic hydrogen additions to radical sites, which are in fact barrierless.

Structure	Energy		Relative Energy		Transition State Energy	
	Hartree		Hartree	kJ mol^{-1}	Hartree	kJ mol^{-1}
a	-662.0837		0.0000	0.0		
					-662.0785	0.0053 13.8
b	-662.0936		-0.0099	-25.9		
					-662.0537	0.0300 78.9
c	-662.0613		0.0225	59.0		
					-662.0368	0.0469 123.3
d	-662.0555		0.0283	74.2		
					-662.0363	0.0475 124.6
e	-662.0477		0.0361	94.7		
					-662.0381	0.0456 119.8
f	-662.0493		0.0344	90.4		
					-662.0150	0.0688 180.6
g	-662.0624		0.0213	56.0		
					-662.0506	0.0332 87.1
h	-662.0613		0.0224	58.8		
					-662.0542	0.0296 77.7
i	-662.1130		-0.0293	-76.9		
j	-662.2765		-0.0179	-46.9		
k	-662.1446		-0.0609	299.5		

Appendix G

Tables showing the energies of gaseous reactants calculated using density functional theory with the B3LYP/6-31G (d) basis set.

Species	Energy	
	Hartree	kJ mol^{-1}
H	-0.5003	-3086.2
H ₂	-1.1755	-1313.5
CH ₃	-39.8358	-104588.8

